





Stone Skipping Black Holes in Ultralight Dark Matter Solitons

Alan Zhang ^{1,*} Yourong Wang ^{2,†} J. Luna Zagorac ^{3,4,‡} and Richard Easther ^{5,§}

¹*Center for Gravitational Astrophysics, Research School of Physics & Research School of Astronomy and Astrophysics, Australian National University, Canberra ACT 2601, Australia*

²*Institut für Astrophysik, Georg-August-Universität Göttingen, D-37077 Göttingen, Germany*

³*Perimeter Institute for Theoretical Physics, 31 Caroline St. N, Waterloo, ON N2L2Y5, Canada*

⁴*Department of Physics & Trottier Space Institute, McGill University, Montréal, QC H3A 2T8, Canada*

⁵*Department of Physics, University of Auckland, Private Bag 92019, Auckland, New Zealand*

(Dated: April 6, 2026)

The orbit of a black hole moving within an ultralight dark matter (ULDM) soliton is naively expected to decay due to dynamical friction. However, single black holes can undergo “stone skipping”, with their orbital radius varying quasi-periodically. We show that stone skipping is induced by the dipole excitation of the soliton. We model it as resonance in a forced, damped harmonic oscillator, demonstrating that the coherent response of the soliton can significantly modify the dynamics of objects orbiting within it. This suggests that a dipole perturbation of a soliton can modify inspiral timescales if the black hole masses are significantly less than the soliton mass, with implications for supermassive black hole dynamics, the final parsec problem and gravitational wave observations in a ULDM cosmology.

I. INTRODUCTION

Identifying the nature of dark matter is a key challenge for astrophysics and fundamental science. On cosmological scales, Cold Dark Matter (CDM), which is embedded within the Λ CDM paradigm, successfully describes the formation of large-scale structure and the anisotropies in the cosmic microwave background [1–4]. However, tensions at galactic and sub-galactic scales motivate candidates with more complicated dynamics than pure CDM. These small-scale challenges include the cusp-core [5–7], missing satellites and the too-big-to-fail problems [8–10]. Baryonic feedback mechanisms may alleviate these discrepancies but models that naturally suppress small-scale power continue to be interesting [11–13].

Ultralight Dark Matter (ULDM), also known as Fuzzy Dark Matter, is one such scenario [14–18]. In these models dark matter consists of extremely light bosonic particles with masses in the range $m \sim 10^{-23}$ – 10^{-19} eV and de Broglie wavelengths up to kiloparsec scales. Such ultralight scalars arise naturally in string theory where the compactification of extra dimensions generically yields a plenitude of axion-like particles [19–21].

The astrophysical behaviour of ULDM is governed by the Schrödinger–Poisson equation [22, 23]. A key prediction of this framework is the presence of solitons, stable, self-gravitating ground-state configurations, at the centers of collapsed halos [24–27]. These solitons are supported by quantum pressure and are surrounded by a halo of fluctuating granules which exhibit wave-like mutual interference [28, 29]. Observational con-

straints from the Lyman- α forest typically imply $m \gtrsim 10^{-21}$ eV [30–32]. Stellar-dynamical heating constraints from the smallest ultra-faint dwarfs can yield substantially stronger limits, $m \gtrsim 10^{-19}$ eV, with the precise value sensitive to modeling assumptions [33–35].

A key arena for ULDM dynamics is the interaction between solitonic cores and the supermassive black holes (SMBHs) that appear to be present at the centers of all large galaxies. A massive object moving through a background medium experiences dynamical friction, a drag force caused by the object’s gravitational wake [36–38]. In ULDM environments, however, the wave-mechanical nature of the medium introduces qualitatively new effects [16, 39, 40]. Unlike collisionless or gaseous backgrounds [41, 42], the coherent response of the condensate can produce oscillatory wakes and feedback loops which are not captured by Chandrasekhar-type formulae [43–47]. Specifically, Wang and Easther [44] demonstrated that a black hole orbiting inside a soliton excites coherent modes that backreact on the trajectory. This leads to “stone skipping,” a non-monotonic secular evolution of the orbital radius. Boey et al. [45] further confirmed that soliton backreaction induces “reheating” that transfers kinetic energy back to the black hole.

The implications of stone skipping the evolution of SMBH binaries are ambiguous. Equal-mass binary SMBH are not subject to stone skipping [45] and in very massive galaxies ULDM may damp orbital motion to the extent that gravitational wave emission in the pulsar timing band [48–51] is suppressed [52]. More broadly, this has implications for the “final parsec problem,” which describes the tendency of SMBH binaries to stall at separations where gravitational-wave emission is inefficient [53–55]. While mechanisms such as stellar hardening and gas torques have been proposed to bridge this gap [56–58], ULDM and related dark-sector effects, including dynamical friction, have also been suggested as possible aids to

* Alan.Zhang1@anu.edu.au

† yourong.wang@uni-goettingen.de

‡ luna.zagorac@mcgill.ca

§ r.easther@auckland.ac.nz

binary hardening [59–62]. However, it also seems soliton backreaction can slow orbital decay in some circumstances. Consequently, it is well worth understanding the detailed dynamics of stone skipping, both for their intrinsic interest and their implications for SMBH dynamics.

We find that stone skipping is driven by the dipole perturbations of the soliton. The dipole response of self-gravitating systems has long been recognized as a source of weakly damped oscillations, which are often referred to as seiche modes, in classical stellar dynamics [63–66]. Our work extends this physical picture to the wave-mechanical context of ULDM via the eigenmode decomposition framework developed by Zagorac et al. [67]. Through controlled simulations with selectively excited or suppressed modes, we establish that dipole terms are both necessary and sufficient to trigger stone skipping. We then model this phenomenon as a resonance in a forced, damped oscillator. The time-dependent dipole provides periodic driving, while dynamical friction acts as dissipation. When the forcing frequency approaches the natural epicyclic frequency the system enters a resonance window where energy transfer from the soliton can overcome secular damping.

The structure of this paper is as follows. Section II introduces the ULDM-black hole system governed by the Schrödinger-Poisson equations and presents a modified formulation in which the black hole is treated as a test particle. Section III describes the eigenmode decomposition of the ULDM wave function in terms of expansion coefficients $c_{nlm}(t)$ and Section IV describes their values in simulations with both single and binary black holes. In Section V we treat the black hole as a test particle and systematically add excited modes to confirm that the dipole modes as the key ingredient for stone skipping. Section VI develops a semi-analytic model that interprets stone skipping as a classical forced, damped oscillator. Section VII presents our conclusions.

II. ULDM DYNAMICS

ULDM can be modeled as a dilute bosonic condensate or superfluid on macroscopic scales [16, 17, 43]. Its dynamics are governed by the Schrödinger-Poisson system,

$$i\hbar\frac{\partial\Psi}{\partial t} = \left[-\frac{\hbar^2}{2m}\nabla^2 + m(\Phi_U + \Phi_E) \right] \Psi, \quad (1)$$

$$\nabla^2\Phi_U = 4\pi Gm|\Psi|^2,$$

where $\Psi(\mathbf{r}, t)$ is the macroscopic wave function and $n(\mathbf{r}, t) = |\Psi(\mathbf{r}, t)|^2$ is the particle number density. The ULDM particle mass is taken to lie in the range $m \sim 10^{-23}$ – 10^{-19} eV [15–17]. The gravitational potentials Φ_U and Φ_E denote the ULDM gravitational potential and that of all other masses in the system, respectively. In our case these are black holes, which we treat as Plummer

spheres with potential

$$\Phi_{BH}(r) = -G\frac{M_{BH}}{\sqrt{r^2 + a^2}}, \quad (2)$$

in numerical simulations where a is the Plummer radius and M_{BH} is the mass. The general equations of motion are

$$\ddot{\mathbf{r}}_{BH,i} = -\nabla\Phi_U(\mathbf{r}_{BH,i}) - \sum_{j \neq i} \nabla\Phi_{BH,j}(\mathbf{r}_{BH,i}), \quad (3)$$

but we are primarily interested in systems with one or two black holes.

Our focus is the interactions between black holes and the ULDM solitons which form naturally at the centers of ULDM halos [24, 25]. The soliton profile cannot be obtained in closed-form but is well approximated by [24]

$$\rho_s(r) \approx \frac{1.9(m/10^{-23}\text{eV})^{-2}(r_c/\text{kpc})^{-4}}{\left[1 + 9.1 \times 10^{-2}(r/r_c)^2\right]^8} M_\odot \text{pc}^{-3}, \quad (4)$$

where r_c is the core radius, defined by $\rho_s(r_c) = \rho_s(0)/2$.

We employ both numerical simulations and expansions of the soliton in terms of its eigenmodes. Simulations are performed with the pseudospectral code PYULTRALIGHT [43, 44]; the expansion is developed in Ref. [67]. Our starting configurations are a soliton and one or two black holes in circular orbits about the overall center of mass.

Unless stated otherwise, the simulations here employ a canonical set of parameters: ULDM particle mass of 10^{-21} eV and a soliton of total mass $M_{\text{tot}} \approx 1.2 \times 10^7 M_\odot$, corresponding to a half-mass radius of $r_c \approx 198.4$ pc evolved in a box of radius $r_{\text{max}} = 2500$ pc for a physical duration of 3000 Myr. The spatial resolution is $N = 128$ with black hole(s) initialized on circular orbits at a radius of 140 pc. We have verified that our results are robust against changes in resolution and the box size.

The naïve expectation is that dynamical friction [36, 37, 44, 45] will reduce the orbital radius of the black hole so it “sinks” to the center of the soliton, and this indeed happens initially. However, at some point the inspiral reverses and the orbital radius increases significantly and the cycle repeats. This behavior is clearly due to the black hole interacting with the now-oscillating soliton, which is excited by the transfer of energy from the orbiting black hole. Stone skipping trajectories are illustrated in Figure 1.

The analysis is challenging because the black hole continuously excites the soliton as it moves within it. We separate these two aspects of the dynamics by simulating the motion of test particles in an excited soliton with an empirical drag term, “turning off” the backreaction of the black hole on the soliton. The excited soliton has the general form

$$\tilde{\rho}_s(\mathbf{r}) = \rho_s(r) + \delta\rho(\mathbf{r}). \quad (5)$$

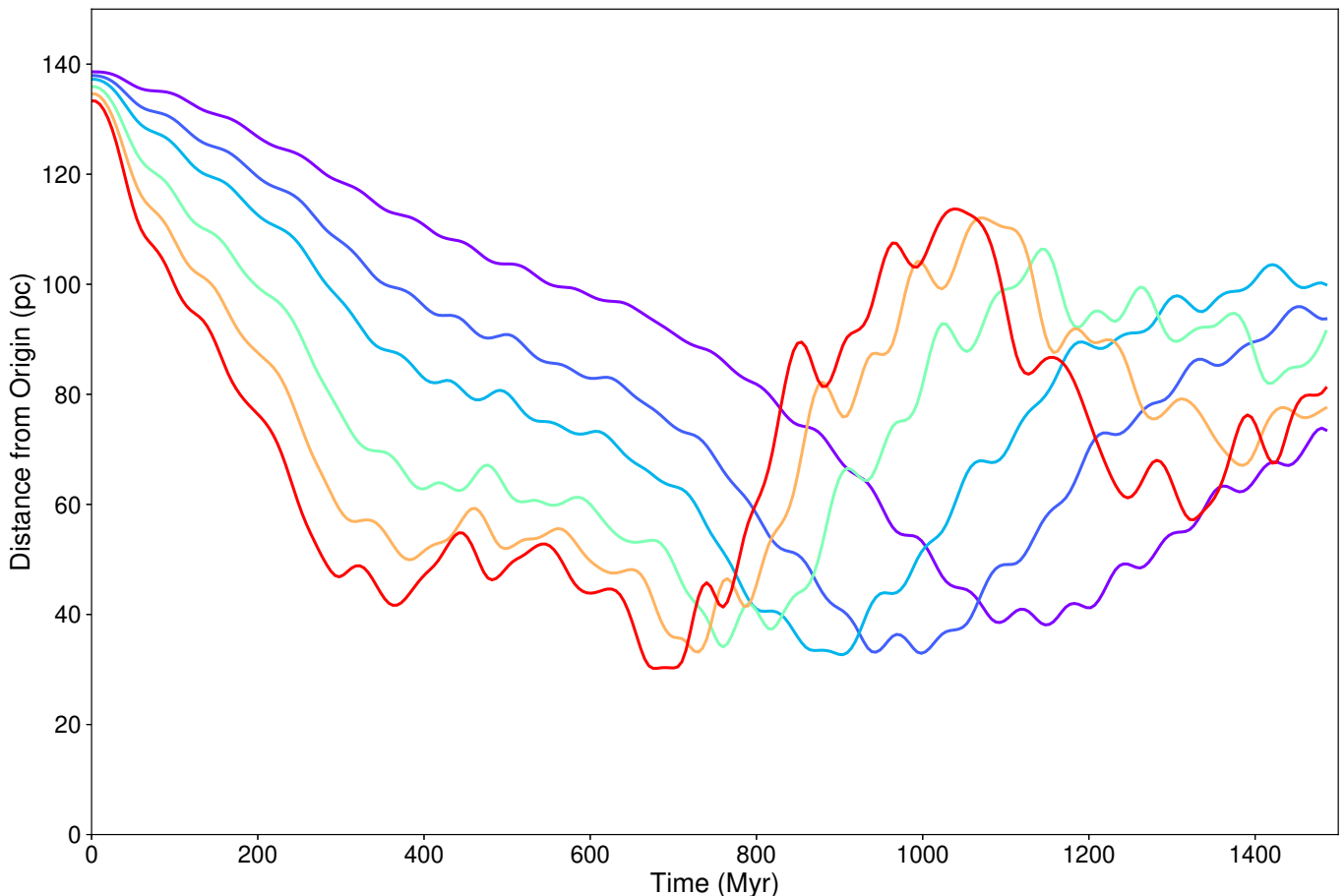


FIG. 1. Time evolution of the orbital radius of black holes in initially circular orbits and masses 1, 1.5, 2, 3, 4 and 5% of the soliton mass, from top to bottom at $t = 0$. The initial orbital radii differ because, while the initial separation between the black hole and the soliton centroid is fixed at 140 pc, more massive black holes lie closer to the system's center of mass. The physical radius of the simulation box is 1.25 kpc.

where $\rho_s(r)$ is the ground state and $\delta\rho(\mathbf{r}, t)$ can be expressed via the eigenmode expansion. The equation of motion becomes

$$\ddot{\mathbf{r}}_{BH,i} = -\nabla\tilde{\Phi}_U(\mathbf{r}_{BH,i}) - \sum_{j \neq i} \nabla\Phi_{BH,j}(\mathbf{r}_{BH,i}) + \frac{1}{M_{BH}} \mathbf{f}(\mathbf{r}_{BH,i}, t), \quad (6)$$

where $\tilde{\Phi}_U$ is ULDM self-potential evolved with $\Phi_E = 0$, to distinguish it from Φ_U in Eq. (3) and $\mathbf{f}(\mathbf{r}_{BH}, t)$ is an empirical drag force. This is adapted from the $kr \ll 1$ limit of the standard approximate expression for the dynamical friction [16, 44],

$$\mathbf{f}(\mathbf{r}_{BH}, t) = -4\pi G^2 A \rho(\mathbf{r}_{BH}, t) \times \frac{M_{BH}^2 m^2 |\mathbf{r}_{BH}|^2 \mathbf{v}_{rel}}{3\hbar^2 |\mathbf{v}_{rel}|}, \quad (7)$$

where $\rho(\mathbf{r}_{BH}, t)$ is the ULDM density evaluated at the BH position \mathbf{r}_{BH} at time t and $\mathbf{v}_{rel} = \mathbf{v}_{BH} - \mathbf{v}_{ULDM}$ is the black hole velocity relative to the ULDM flow

field. Finally, A is a dimensionless constant of order unity which is adjusted empirically to reproduce the drag force seen in simulations. We have implemented these capabilities in a branch of PYULTRALIGHT.¹

III. EIGENMODE DECOMPOSITION

Our approach is based on Ref. [67] which we generalize to include the full set of angular states. The macroscopic ULDM wave function is equivalent to an effective single-particle wave function up to its normalization so we may construct eigenmodes using standard quantum-mechanical methods. In operator form the Schrödinger

¹ The PYULTRALIGHT fork used in this work is available at https://github.com/Ailun-Zhang/PyUL_SK. The post-processing and visualization scripts used to analyse the PYULTRALIGHT wavefunction outputs are available at <https://github.com/Ailun-Zhang/ULDM-Eigenmode-Toolkit>.

sector of the system is

$$i\hbar \frac{\partial}{\partial t} |\Psi\rangle = \hat{H}(t) |\Psi\rangle, \quad \hat{H}(t) = \hat{H}_0 + \hat{V}(t), \quad (8)$$

where we separate a time-independent part from a time-dependent perturbation. The unperturbed Hamiltonian \hat{H}_0 consists of the usual kinetic term and the gravitational potential Φ_0 of the ground-state soliton

$$\hat{H}_0 = -\frac{1}{2}\nabla^2 + \Phi_0. \quad (9)$$

The eigenstates are defined via the time-independent Schrödinger equation,

$$\hat{H}_0 |n, \ell, m\rangle = E_{n\ell} |n, \ell, m\rangle, \quad (10)$$

where (n, ℓ, m) are the usual quantum numbers. Eq. (10) is spherically symmetric so, as usual, separation of variables yields

$$\psi_{n\ell m}(\mathbf{r}) = \langle \mathbf{r} | n, \ell, m \rangle = f_{n\ell}(r) Y_{\ell m}(\theta, \phi), \quad (11)$$

where $Y_{\ell m}$ are the orthonormal spherical harmonics. The radial functions have no simple closed form but satisfy

$$\left[-\frac{1}{2} \frac{d^2}{dr^2} + \frac{\ell(\ell+1)}{2r^2} + \Phi_0(r) \right] u_{n\ell}(r) = E_{n\ell} u_{n\ell}(r), \quad (12)$$

$$u_{n\ell}(r) \equiv r f_{n\ell}(r),$$

with boundary conditions $u_{n\ell}(0) = u_{n\ell}(r_{\max}) = 0$. Figure 2 shows examples of the radial eigenfunctions for $n \leq 4$ and $\ell \leq 2$.

As described in Appendix A, we must solve the radial problem numerically and the resulting eigenvectors are chosen to be orthonormal and complete in the discretized space. The eigenstates satisfy

$$\langle n', \ell', m' | n, \ell, m \rangle = \delta_{nn'} \delta_{\ell\ell'} \delta_{mm'}, \quad (13)$$

$$\sum_{n\ell m} |n, \ell, m\rangle \langle n, \ell, m| = \mathbb{I}. \quad (14)$$

The eigenstates Eq. (10) are constructed for the ground-state soliton background and are not eigenstates of the full time-dependent Hamiltonian in Eq. (1) with its non-trivial external potential. Nevertheless, because they form a complete basis in the Hilbert space $L^2(\mathbb{R}^3, \mathbb{C})$, they can be used to expand the ULDM wave function at arbitrary times after it is perturbed by a black hole. We introduce an effective single-particle wave function

$$\psi(\mathbf{r}, t) = \frac{1}{\sqrt{N}} \Psi(\mathbf{r}, t), \quad N = \int d^3\mathbf{r} |\Psi|^2, \quad (15)$$

since the eigenstates (11) are normalized in the single-particle sense, whereas the macroscopic field Ψ carries a different normalization and statistical meaning.²

We expand the macroscopic ULDM wave function

$$\Psi(\mathbf{r}, t) = \sqrt{M_{\text{tot}}} \sum_{n\ell m} c_{n\ell m}(t) \psi_{n\ell m}(\mathbf{r}), \quad (16)$$

where $c_{n\ell m}(t)$ are complex, time-dependent coefficients and $M_{\text{tot}} = Nm$ is the total soliton mass. The ground state $|0, 0, 0\rangle$ corresponds to the soliton itself. In the small-perturber regime (which applies here with black hole masses at the few-percent level) the ULDM field is a combination of the ground state and a small number admixture of excited modes.

States with $\ell > 0$ are aspherical, while those with $\ell = 0$ and $n \neq 0$ are purely radial. In analogy with multipole terminology, we further define, for each n ,

$$\text{Monopole: } c_{000} \psi_{000}, \quad (17)$$

$$\text{Dipole: } \sum_{m=-1}^1 c_{n1m} \psi_{n1m}, \quad (18)$$

$$\text{Quadrupole: } \sum_{m=-2}^2 c_{n2m} \psi_{n2m}. \quad (19)$$

IV. SOLITON EXCITATIONS FROM STONE SKIPPING

As usual, the orthonormality (13) yields

$$c_{n\ell m}(t) = \frac{1}{\sqrt{M_{\text{tot}}}} \int d^3\mathbf{r} \Psi(\mathbf{r}, t) \psi_{n\ell m}^*(\mathbf{r}). \quad (20)$$

In this mean-field setting, $|c_{n\ell m}(t)|^2 \lesssim 1$ can be interpreted as the fractional occupation (by mass/number) of the mode $\psi_{n\ell m}$ at time t . Since the black hole is much less massive than the soliton we expect the soliton to remain close to its ground state, *i.e.* $|c_{000}(t)|^2 \simeq 1$ and other coefficients much less than unity, and this is confirmed for a range of parameter choices.

We decompose time-dependent ULDM wave functions obtained from simulations initialized with the pure-soliton profile for three configurations: (i) a control run with no black hole, (ii) a binary where each black hole is 2% of the soliton mass. (iii) a single black hole that is 2% of the soliton mass. The binary evolution is shown in Figure 3, consistent with Refs [59, 61] the black hole radii decrease steadily but not strictly monotonically, in contrast to the stone skipping shown in Figure 1.

The top row of Figure 4 shows the decomposition of the pure soliton; as expected it is almost time independent. Aside from the monopole component (the soliton itself) there are small $\ell = 0$ radial excitations with $n \neq 0$ which likely correspond to a slight mismatch in the initial profile and aspherical components remain below $\sim 10^{-12}$, consistent with numerical noise. The middle row shows the equal-mass binary; the quadrupole is excited, reaching a fractional contribution of $\sim 10^{-5}$ for $n = 0$ and the dipole remains small. The bottom row is the single

² The macroscopic wave function output by PYULTRALIGHT includes a factor of \sqrt{m} , and is related to the field appearing in Eq. (1) by $\Psi_{\text{PYUL}} = \sqrt{m} \Psi$. In the “code units” $c = \hbar = G = m = 1$ this distinction disappears.

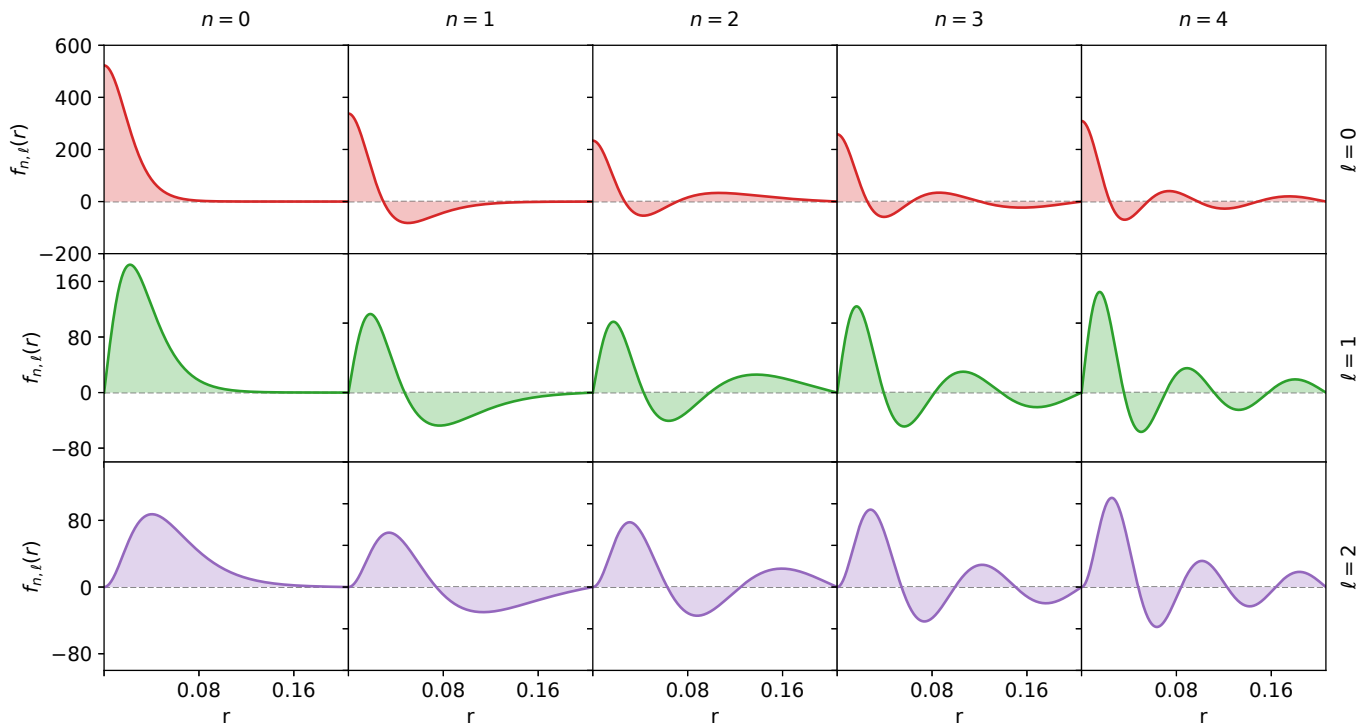


FIG. 2. ULDM radial eigenfunctions with $n \leq 4$ and $\ell \leq 2$. The quantum number n sets the number of radial nodes, while ℓ determines the small- r asymptotic behavior, $f_{n\ell}(r) \propto r^\ell$ as $r \rightarrow 0$. Modes with the same ℓ are shown using the same color ($\ell = 0$ in red, $\ell = 1$ in green, and $\ell = 2$ in purple); the same convention is adopted in subsequent figures.

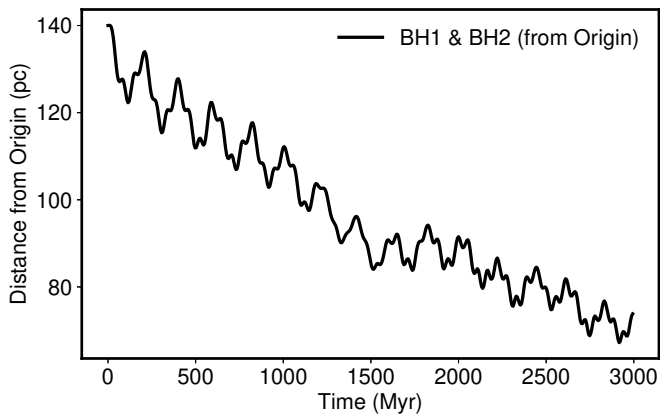


FIG. 3. Evolution of the orbital radii of an equal-mass black hole binary, black hole masses are 2% of the soliton mass.

black hole case and both dipole and quadrupole components are appreciably excited with the dipole dominant; for $n = 1$, the weight rises to ~ 0.004 .

In particular, the mode $|n = 1, \ell = 1, m = -1\rangle$ is not only the largest aspherical component but is roughly periodic in time.³ We plot it separately on linear axes in

Figure 5 and can describe it phenomenologically via

$$|c_{1,1,-1}(t)|^2 \sim C \cos^2(\omega_{\text{dip}} t + \phi_0), \quad (21)$$

where C sets the amplitude, ω_{dip} is the dipole oscillation frequency, and ϕ_0 is an initial phase.⁴ This oscillation can be interpreted as the effective driving force in a forced, damped oscillator model for stone skipping. To specify the driving term more fully we must analyze the frequency content of the *complex* coefficient $c_{1,1,-1}(t)$ (without taking the modulus) and infer a plausible functional form from its spectrum.

Note that the coefficients are continuously modified by the interaction between the soliton and the black hole potential—if these were pure eigenstates we would expect the amplitudes to be roughly constant. Some spherically symmetric radial modes ($\ell = 0$, $n \neq 0$) can attain amplitudes comparable to the dipole modes. As shown in Figure 6, such a radial component displays the same qualitative oscillatory pattern and a similar amplitude, but with a higher oscillation frequency.

While radial modes are excited in both single and binary black hole scenarios, significant dipole excitation is

³ The asymmetry between the $m = \pm 1$ modes reflects the orbital direction of the black hole; if we reverse the direction the $m = 1$ mode is larger.

⁴ The overall amplitude decays if the simulation is run for very long times. However, the decay rate decreases with increasing resolution, so this appears to be a numerical artifact, at least in part.

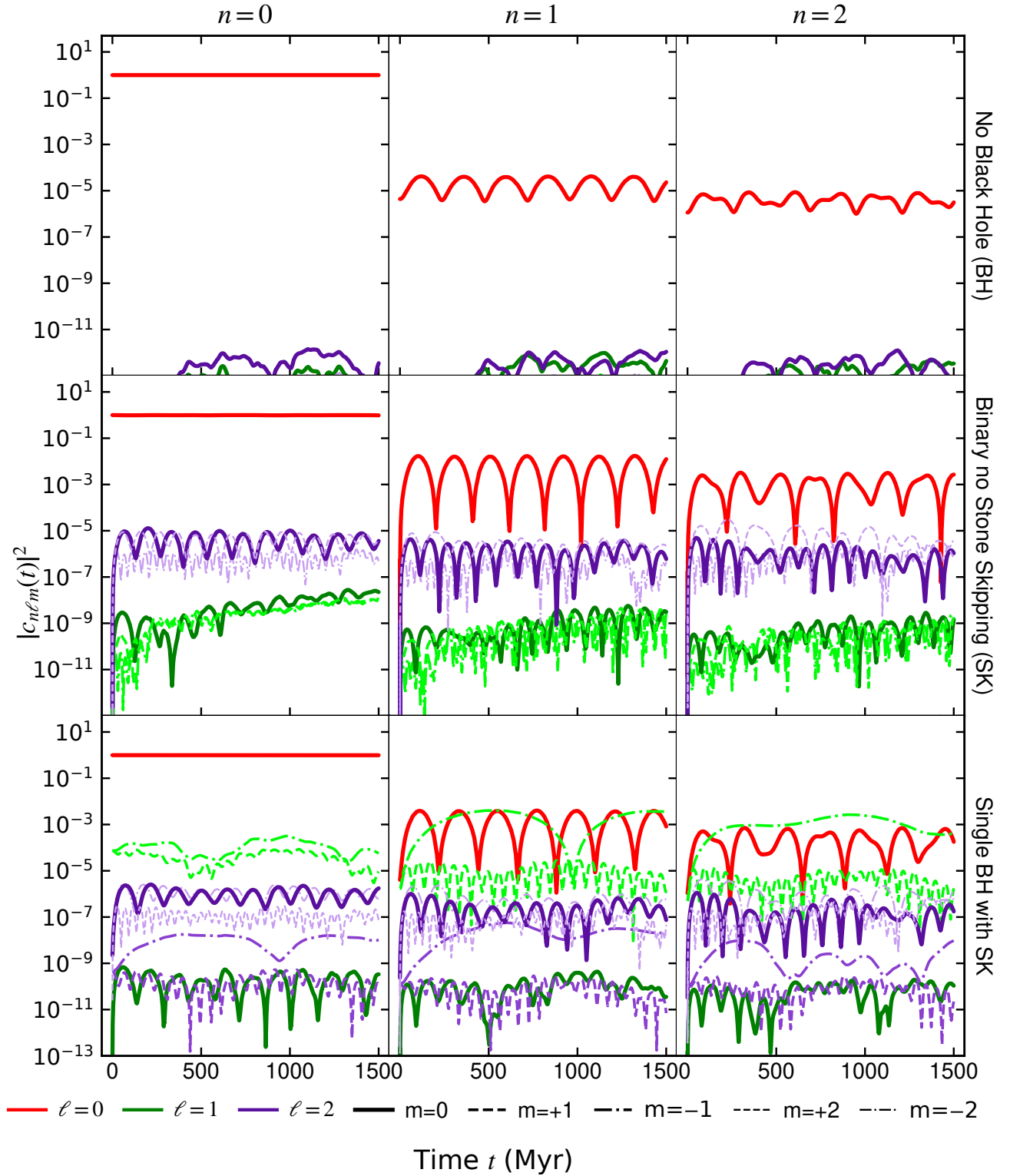


FIG. 4. The of $|c_{n\ell m}(t)|^2$ obtained from the eigenmode decomposition of the ULDM wave functions. Top row: pure soliton without a black hole. Middle row: soliton with an equal-mass binary with each black hole mass 2% of the soliton mass; no stone skipping observed. Bottom row: single black hole with mass 2% of the soliton mass; stone skipping observed. Colors denote mode groups: red for the monopole, green for the dipole, and purple for the quadrupole; within each group, shading lightens as $|m|$ increases. Line styles distinguish the azimuthal order m : thick solid curves for $m = 0$, dashed for $m > 0$, and dash-dotted for $m < 0$, with line width decreasing as $|m|$ increases.

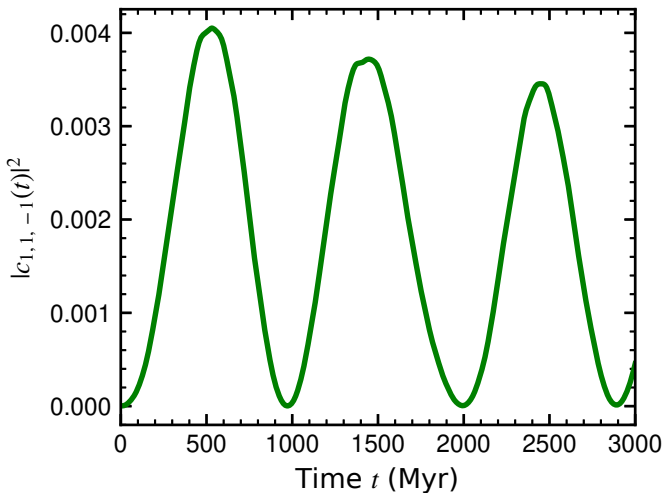


FIG. 5. Evolution of the dipole component $|c_{1,1,-1}(t)|^2$ in the stone skipping run perturbed by a single black hole. The curve is well described by a \cos^2 -type oscillation.

unique to the single black hole case. This suggests that the dipole interaction is the primary driver of stone skipping. We test this hypothesis below by evolving black holes in controlled backgrounds where either radial or dipole modes are selectively excited.

V. EIGENMODES AND STONE SKIPPING

A sharper test of the correlation between ULDM excitations and stone skipping is to construct initial ULDM states containing specific eigenmodes while and evolving the black hole via Eq. (6) with the empirical drag Eq. (7). More specifically,

$$\Psi_{\text{init}}^{\vec{v}_0} = \sqrt{M_{\text{tot}}} \sum_{n=0}^N \sum_{\ell=0}^L \sum_{m=-\ell}^{\ell} c_{nlm}(t_0) |n, \ell, m\rangle \quad (22)$$

for some (typically small) values of N and L and with c_{000} is much bigger than the others. We ensure that M_{tot} is actually the total mass by rescaling the “raw” monopole term \bar{c}_{000}

$$c_{000} = \frac{\bar{c}_{000}}{|\bar{c}_{000}|} \sqrt{1 - \sum_{n,\ell,m \neq 0} |c_{nlm}|^2}. \quad (23)$$

The superscript \vec{v}_0 in Eq. (22) indicates that the configuration generally carries a bulk (center-of-mass) velocity,

$$\vec{v}_0 = \frac{\hbar}{m} \frac{\int d^3r \operatorname{Im} \left[\left(\Psi_{\text{init}}^{\vec{v}_0} \right)^* \nabla \Psi_{\text{init}}^{\vec{v}_0} \right]}{\int d^3r \left| \Psi_{\text{init}}^{\vec{v}_0} \right|^2}. \quad (24)$$

A Galilean boost

$$\Psi_{\text{init}}^0 = \exp \left(-\frac{i}{\hbar} m \vec{v}_0 \cdot \vec{r} \right) \Psi_{\text{init}}^{\vec{v}_0}. \quad (25)$$

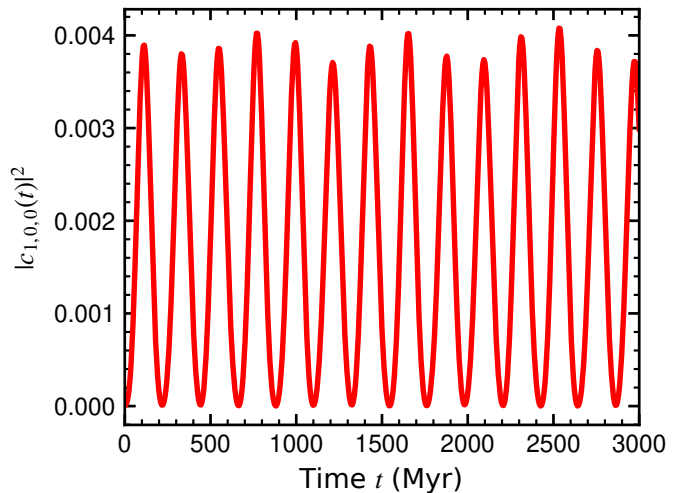


FIG. 6. Evolution of the radial component $|c_{1,0,0}(t)|^2$ in the stone skipping run perturbed by a single black hole. The curve is approximately \cos^2 -like.

thus keeps the ULDM center of mass at the origin.

We construct Ψ_{init}^0 from subsets of the c_{nlm} to isolate the terms responsible for stone skipping. We include radial modes ($\ell = 0$) up to n_r and dipole modes c_{n1m} with $n \leq n_d$. For definiteness we fix $t_0 = 2,500$ Myr and then the c_{nlm} accordingly. The drag coefficient is chosen to be $A = 0.75$; this gave the best qualitative fit to the full dynamics. Note too that these simulations will roughly constant $|c_{nlm}|^2$; the \cos^2 modulation in the full simulations is induced by forcing from the black holes and this suppressed in this approximation. Crucially, this does not imply a static potential, as the time evolution is determined by the real part of the coefficients (see Eq. B13 in Appendix B). Figure 7 shows that the stone skipping is only present when the dipole modes are excited and does not require that the radial modes are excited.

These results also explain the absence of stone skipping for equal-mass binaries in fully coupled simulations. As seen in the second row of Figure 4 an equal-mass binary does not appreciably excite the dipole sector and the absence of stone skipping is thus to be expected. However, in realistic astrophysical environments the dipole could be externally excited (e.g. by a merger) component could be seeded by mechanisms other than black hole perturbations would lead to stone skipping. Fig. 8 shows both the uncoupled and fully coupled evolution of an equal mass black hole binary in a soliton with a dipole excitation, and both cases exhibit stone skipping.

VI. A SEMI-ANALYTIC RESONANCE MODEL

We now develop a semi-analytic model of stone skipping. In this picture, the time-dependent gravitational field induced by the evolution of the dipole excitation is

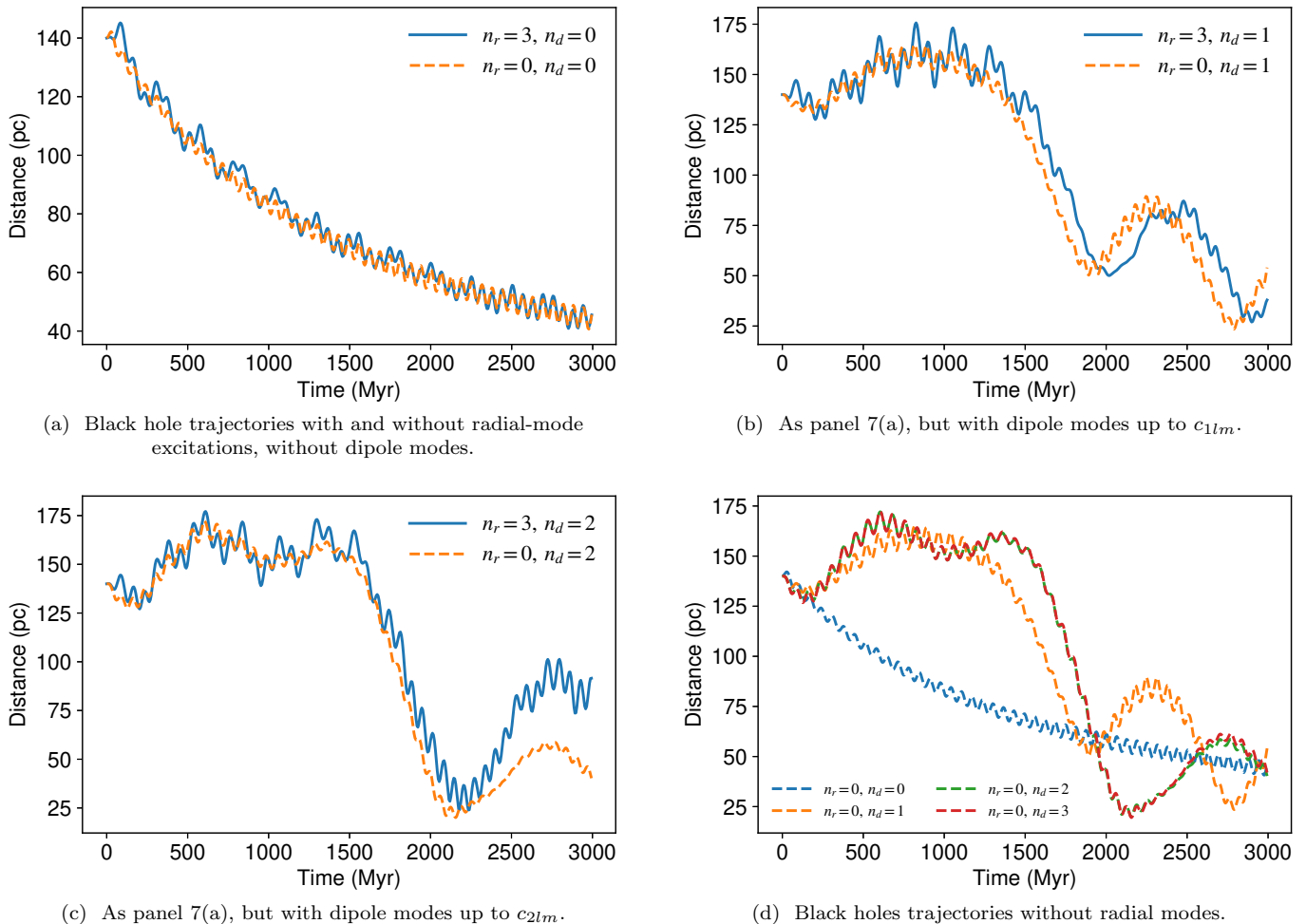


FIG. 7. Comparisons of black hole trajectories with (orange) and without (blue) radial-mode excitations at fixed dipole content; n_r denotes the maximum radial quantum number and n_d denotes the maximum n included in the dipole modes.

as an external driving force while the dynamical friction experienced by a black hole provides dissipation.

Concretely, we write the equations of motion for a black hole confined to a two-dimensional plane in a background consisting of the soliton plus a single excited mode of amplitude ϵ , and include the effective dynamical-friction prescription (Eq. (7)). In polar coordinates, the dynamical friction is taken to be proportional to two damping coefficients, γ_r and γ_ϕ , for the radial and azimuthal components, respectively. We then expand the equations about a circular orbit,

$$r(t) = r_0 + \xi(t), \quad \phi(t) = \Omega_0 t + \eta(t), \quad (26)$$

where (r, ϕ) are the black hole coordinates, r_0 is the circular-orbit radius, Ω_0 is the corresponding orbital frequency, and $\xi(t)$ and $\eta(t)$ are first-order perturbations about the circular solution. This procedure yields a linear system of differential equations for (ξ, η) .

We first consider the conservative limit in which both the excited mode and dynamical friction are switched off, *i.e.* $\epsilon = \gamma_r = \gamma_\phi = 0$. After the change of variables

$\xi = u$, the linearized system reduces to a simple harmonic oscillator,

$$\ddot{u} + \kappa^2 u = 0, \quad (27)$$

where κ is the epicyclic frequency of the soliton–black hole system. It is determined by the local soliton potential and the orbital frequency,

$$\kappa^2 = \Phi_0''(r_0) + 3\Omega_0^2. \quad (28)$$

If we turn on the excited mode while keeping dynamical friction switched off, the same transformation leads to a forced harmonic oscillator,

$$\ddot{u} + \kappa^2 u = F(t), \quad (29)$$

where $F(t)$ is a driving term set by the oscillation frequency of the excited mode. For the coefficient $c_{1,1,-1}(t)$, which we found to be most strongly associated with stone skipping, a Fourier analysis of the simulation data indicates a prominent splitting into two comparably strong

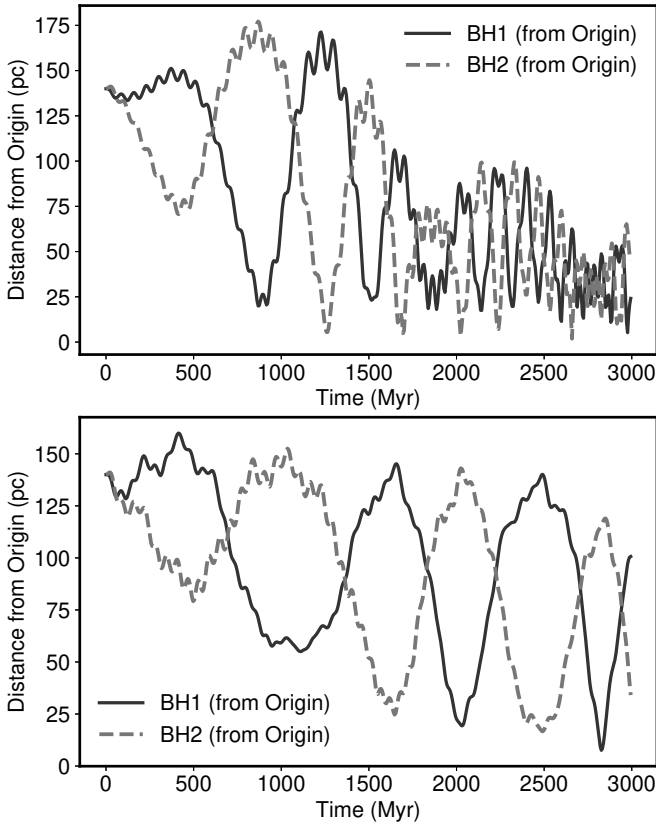


FIG. 8. Orbital-radius evolution of an equal-mass binary (each black hole has mass 2% of the soliton mass) in a soliton+dipole background. The top plot shows the results of the effective dynamical-friction prescription with black hole \rightarrow ULDM coupling switched off; the lower plot shows the full coupled solution. In both cases stone skipping behavior is clearly apparent.

frequency peaks, suggestive of an effective level splitting. Figure 9, the two dominant frequencies are

$$\begin{aligned} f_1 &= 0.000999983 \text{ Myr}^{-1}, \\ f_2 &= -0.000233329 \text{ Myr}^{-1}, \end{aligned} \quad (30)$$

with a separation

$$\Delta f = f_2 - f_1 = 1.23 \times 10^{-3} \text{ Myr}^{-1}. \quad (31)$$

Empirically, Δf coincides with the strongest nonzero frequency in the envelope of $|c_{1,1,-1}(t)|$, which we denote by the envelope (dipole) angular frequency,

$$\omega_{\text{dip}} \equiv \frac{\omega_2 - \omega_1}{2}. \quad (32)$$

as it sets the apparent oscillation frequency of the dipole modes in the time domain. These observations motivate the approximation

$$c_{1,1,-1}(t) \approx A (e^{i\omega_1 t} + e^{i\omega_2 t}) = 2A \cos(\omega_{\text{dip}} t) e^{i\bar{\omega} t}, \quad (33)$$

with carrier frequency

$$\bar{\omega} = \frac{\omega_1 + \omega_2}{2}. \quad (34)$$

Building on this structure, one can derive an explicit expression for the forcing term $F(t)$ (see Appendix B),

$$F(t) = A_1 \sin(\omega_1 t - \Omega_0) + A_2 \sin(\omega_2 t + \Omega_0), \quad (35)$$

where $A_{1,2}$ are amplitudes that respectively depend on $\omega_{1,2}$. In the absence of dynamical friction, the corresponding resonance condition is

$$\omega_{1,2}^2 = \kappa^2 = \Phi_0''(r_0) + 3\Omega_0^2. \quad (36)$$

For the most general case in which both dynamical friction and the excited mode are present, the linearized dynamics can be written as a non-standard higher-order differential equation of the form

$$\ddot{\xi} + (\gamma_\phi + \gamma_r)\dot{\xi} + (\kappa^2 + \gamma_\phi\gamma_r)\xi + \gamma_\phi\kappa^2\xi - 2\gamma_\phi r_0\Omega_0^2 = G(t), \quad (37)$$

where $G(t)$ is more complicated than the forcing term in Eq. (35). While such a system can still exhibit resonant behavior, a complete analysis is beyond the scope of the present work. Instead, we consider an instructive limit: we retain radial damping ($\gamma_r \neq 0$) and the mode excitation ($\epsilon \neq 0$), but switch off azimuthal damping by setting $\gamma_\phi = 0$. In this limit we have a standard forced, damped harmonic oscillator,

$$\ddot{u} + 2\Gamma\dot{u} + \kappa^2 u = F(t), \quad (38)$$

with $\Gamma = \gamma_r/2$.

For the canonical monochromatic forcing problem

$$\ddot{u} + 2\Gamma\dot{u} + \kappa^2 u = F(\omega), \quad (39)$$

the non-decaying steady-state response takes the form

$$\xi(\omega) = \frac{(a\omega + b) \sin(\omega t + \delta - \frac{\pi}{2})}{\omega \sqrt{(\kappa^2 - \omega^2)^2 + (2\Gamma\omega)^2}}, \quad (40)$$

where δ is the phase of the complex amplitude. If $0 < \omega \ll -\frac{2\Omega_0\Phi_{1m}(r_0)}{r_0\Phi'_{1m}(r_0)}$ (see Appendix B), one obtains the resonance condition

$$\omega^2 = \frac{4\kappa^2}{3} \left[\frac{1}{2} - \left(\frac{\Gamma}{\kappa}\right)^2 + \sqrt{\left(\left(\frac{\Gamma}{\kappa}\right)^2 - \frac{1}{2}\right)^2 - \frac{3}{16}} \right] \quad (41)$$

where

$$\frac{\Gamma}{\kappa} < \frac{1}{2\sqrt{2+\sqrt{3}}}. \quad (42)$$

In the weak-damping regime this simplifies to

$$\omega^2 \simeq \kappa^2 - 4\Gamma^2, \quad \frac{\Gamma}{\kappa} \ll 1. \quad (43)$$

If $\omega \gg -\frac{2\Omega_0\Phi_{1m}(r_0)}{r_0\Phi'_{1m}(r_0)} > 0$, the resonance condition becomes

$$\omega = \sqrt{\kappa^2 - 2\Gamma^2}, \quad \frac{\Gamma}{\kappa} < \frac{1}{\sqrt{2}} \quad (44)$$

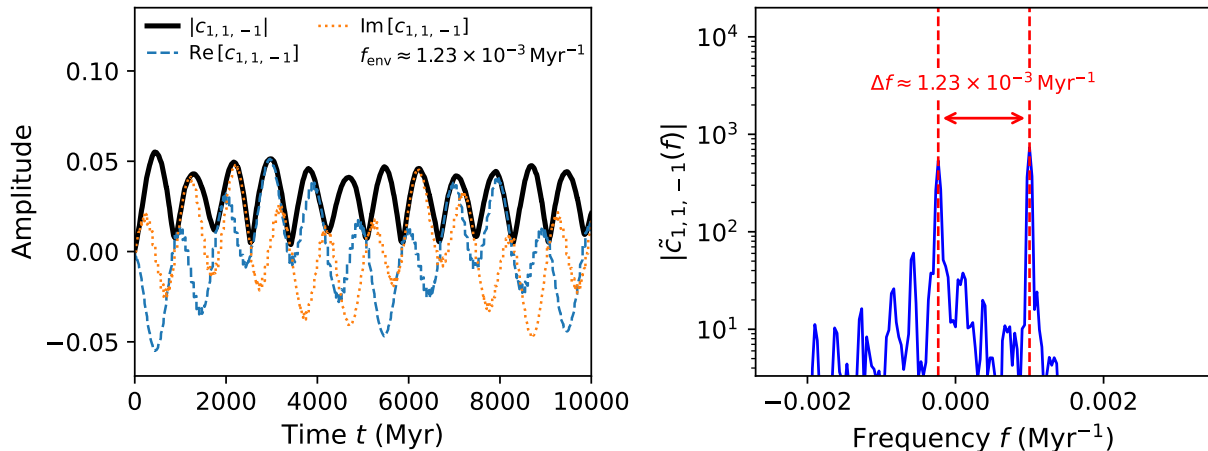


FIG. 9. Spectral analysis of the coefficient $c_{1,1,-1}(t)$. Left: real and imaginary parts in the time domain, together with the dominant envelope frequency f_{env} (corresponding to the angular frequency $\omega_{\text{dip}} = 2\pi f_{\text{env}}$). Right: FFT spectrum showing two strong peaks associated with an apparent splitting. Additional negative-frequency peaks have amplitudes at the $\mathcal{O}(10^{-2})$ level and are neglected.

Because the forcing term $F(t)$ in Eq. (35) contains two frequencies, $\omega_{1,2}$, the system can resonate at either (or both) of these components, leading to a substantial growth of the deviation from circular motion. Within this framework, stone skipping can be interpreted as an orbital resonance driven by the dipole modes. The model also has the potential to explain why other excitations do not generically produce stone skipping. For instance, although radial modes can be strongly excited, their dominant frequencies typically lie outside the range of ω that satisfies the resonance condition (41) for generic ULDM-black hole configurations.

VII. CONCLUSION

We have investigated the orbital dynamics of black holes immersed in ULDM solitons and identified the physical mechanism that drives stone skipping [44], which leads to long-lived quasi-periodic variations in the orbital radius of the black holes. We do this by using an eigenmode decomposition and perturbation theory [67] to show that this behavior is tightly correlated with a dipole-like excitation of the soliton. Simulations with mode-filtered backgrounds confirm that dipole modes are both necessary and sufficient to trigger stone skipping. The result is a dynamical regime in which the soliton backreaction is a central ingredient of the orbital evolution [44, 45].

We developed a semi-analytic model that captures the essential physics. Mapping the dynamics near a reference circular orbit onto a forced oscillator shows that the time-dependent dipole modes yield a periodic driving term while dynamical friction leads to dissipation. Within this framework stone skipping arises when the forcing contains frequency support close to the orbital

(or epicyclic) frequency and the system enters a resonance window in which energy transfer from the excited soliton to the orbit overcomes the secular damping.

Our results make it clear that dynamical friction in ULDM cannot always be treated as a quasi-static Chandrasekhar-type drag with a slowly varying Coulomb logarithm [36, 37] as the coherent soliton response generates time-dependent forces and feedback effects not captured within this approximation [16, 39]. Interestingly, this dipole-driven mechanism has an analogue in classical stellar dynamics where the $\ell = 1$ response of has previously been recognized as a source of weakly damped oscillations, or seiche modes that can significantly affect orbital decay [63–65]. Our findings extend this picture to the wave-mechanical context of ULDM where the coherent condensate can potentially make these resonances more pronounced than in their collisionless counterparts.

This work has particular relevance to SMBH binaries in galactic nuclei where ULDM-enhanced drag might alleviate the final parsec problem and modify the gravitational-wave signals [52, 59, 61]. Our findings show backreaction-driven resonances could qualitatively prolong orbital evolution even though the mean trend is dissipative in stone skipping scenarios. However, full dynamical simulations suggest that stone skipping is not effective in scenarios where the black hole mass is a significant fraction ($\gtrsim 10\%$) of the soliton mass [44]. Consequently, this is mainly relevant to smaller halos which tend to have proportionately smaller SMBH:soliton mass ratios [68]. A pulsar timing stochastic background is likely to be dominated by the largest halos so any observational consequences of stone skipping, in terms of merger rates and associated gravitational wave production, is likely of more relevance to LISA [69]. Conversely, equal-mass binaries are immune to stone skipping provided their evolution begins inside an unperturbed soliton.

Several directions follow naturally. A first priority is to embed the soliton in a more realistic galactic environment by incorporating an outer halo and assessing the impact of ambient ULDM granule fluctuations and relaxation processes [16, 40] on any dipole excitation of the soliton. Second, the resonance model should be generalized to eccentric or inclined orbits and multi-body configurations. Third, given that unequal-mass binaries or mergers could excite a dipole term it will be valuable to delineate the parameter space in which soliton-driven resonance works against a drag-driven inspiral. Fourth, one could generalize this work to models with a mixture of cold and ultralight dark matter [70] and multi-component ULDM models [71–74]. Finally, we did not describe the original excitation of the dipole (and other) modes by the orbiting black hole(s) within perturbation theory – a full treatment of this would be both interesting and useful.

ACKNOWLEDGMENTS

AZ is grateful to Brian Schmidt for his mentorship and guidance, and for facilitating the exchange visit to the University of Auckland where this work was initiated. We thank the Department of Physics at the University of Auckland for its hospitality. We also acknowledge the use of computing resources provided by the Australian National University. RE acknowledges support from the Marsden Fund Council grant MFP-UOA2131 from New Zealand Government funding, managed by the Royal Society Te Apārangi and the use of New Zealand eScience Infrastructure (NeSI) high-performance computing facilities. YW acknowledges the computing time granted by the Resource Allocation Board and provided on the supercomputer Emmy at NHR-Nord@Göttingen as part of the NHR infrastructure. Some simulations were conducted with computing resources under the project nip00084. Research at Perimeter Institute is supported in part by the Government of Canada through the Department of Innovation, Science and Economic Development Canada and by the Province of Ontario through the Ministry of Colleges and Universities. At McGill University LZ is supported by the Trottier Space Institute Fellowship.

Appendix A: Eigenstates of the ULDM soliton

We review the numerical solution of the eigenfunction equations of the time-independent Schrödinger equation (10) for soliton configurations. In this Appendix we set $m = \hbar = G = c = 1$ so Eq. (10) becomes

$$\begin{aligned} \hat{H}_0 |n, \ell, m\rangle &= \left(-\frac{1}{2} \nabla^2 + \Phi_0 \right) |n, \ell, m\rangle \\ &= E_{n\ell} |n, \ell, m\rangle. \end{aligned} \quad (\text{A1})$$

Writing the position representation of the ket $|n\ell m\rangle$ in spherical coordinates as $\psi_{n\ell m}(\mathbf{r})$

$$|n, \ell, m\rangle = \int_{\mathbb{R}^3} d^3\mathbf{r} \psi_{n\ell m}(\mathbf{r}) |\mathbf{r}\rangle. \quad (\text{A2})$$

Taking the $\langle \mathbf{r} |$ derivative of equation (A1) yields:

$$\nabla^2 \psi_{n\ell m}(\mathbf{r}) = 2(\Phi_0 - E_{n\ell}) \psi_{n\ell m}(\mathbf{r}). \quad (\text{A3})$$

Following the standard approach for hydrogen atom wavefunctions, we work in spherical coordinates and employ separation of variables, so that

$$\begin{aligned} \left[\frac{\partial_r (r^2 \partial_r)}{r^2} + \frac{\partial_\theta (\sin \theta \partial_\theta)}{r^2 \sin \theta} + \frac{\partial_\phi^2}{r^2 \sin^2 \theta} \right] \psi_{n\ell m}(r, \theta, \phi) \\ = 2(\Phi_0 - E_{n\ell}) \psi_{n\ell m}(r, \theta, \phi), \end{aligned} \quad (\text{A4})$$

and

$$\psi_{n\ell m}(r, \theta, \phi) = f_{n\ell}(r) \Theta_{\ell m}(\theta) \tilde{\Phi}_m(\phi). \quad (\text{A5})$$

The angular portion yields the condition:

$$\frac{\partial_\theta (\sin \theta \partial_\theta \Theta_{\ell m}(\theta))}{\sin \theta \tilde{\Phi}_m(\phi)} + \frac{\partial_\phi^2 \tilde{\Phi}_m(\phi)}{\sin^2 \theta \Theta_{\ell m}(\theta)} = -\ell(\ell + 1) = C, \quad (\text{A6})$$

where C is a constant. The radial equation becomes:

$$\frac{\partial_r (r^2 \partial_r f_{n\ell}(r))}{r^2 f_{n\ell}(r)} - \frac{\ell(\ell + 1)}{r^2} = 2(\Phi_0 - E_{n\ell}). \quad (\text{A7})$$

The solution to equation (A6) consists of the familiar spherical harmonics:

$$Y_{\ell m}(\theta, \phi) = \sqrt{\frac{(2\ell + 1)(\ell - m)!}{4\pi(\ell + m)!}} (-1)^m P_{\ell m}(\cos \theta) e^{im\phi}. \quad (\text{A8})$$

For the radial component, we solve equation (A7) using a substitution:

$$u_{n\ell}(r) = r f_{n\ell}(r). \quad (\text{A9})$$

This allows us to rewrite:

$$\frac{\partial_r (r^2 \partial_r f_{n\ell}(r))}{r^2} = \frac{1}{r} \frac{\partial^2 u_{n\ell}}{\partial r^2}. \quad (\text{A10})$$

Equation (A7) then transforms to:

$$\frac{\partial^2 u_{n\ell}}{\partial r^2} - \frac{l(l + 1)}{r^2} u_{n\ell}(r) = 2(\Phi_0 - E_{n\ell}) u_{n\ell}(r) \quad (\text{A11})$$

Alternatively, defining $\chi_\ell(r)$ for a more concise form:

$$\begin{aligned} \frac{1}{2} \left(\chi_\ell(r) - \frac{\partial^2}{\partial r^2} \right) u_{n\ell}(r) &= E_{n\ell} u_{n\ell}(r), \\ \chi_\ell(r) &= \ell(\ell + 1)r^{-2} + 2\Phi_0. \end{aligned} \quad (\text{A12})$$

We discretize equation (A12), transforming it into a matrix eigenvalue problem. Note that $u_{n\ell}(r)$ represents a one-dimensional distribution. We impose boundary conditions on the interval $[0, r_{\max}]$, with uniform spacing $\Delta r = r_{i+1} - r_i$, where $i \in \{0, 1, \dots, N, N+1\}$ corresponds to sampling at $N+2$ points, or

$$r_i = i\Delta r, \quad r_i + k\Delta r = r_{i+k}, \quad \Delta r = \frac{r_{\max}}{N+1}. \quad (\text{A13})$$

We can express $u_{n\ell}(r)$ in vector form:

$$u_{n\ell} = [0 \quad u_{n\ell}(r_1) \quad u_{n\ell}(r_2) \quad \dots \quad u_{n\ell}(r_N) \quad 0]^T \quad (\text{A14})$$

The boundary conditions are then

$$u_{n\ell}(r_0) = r_0 f_{n\ell}(r_0) = 0 \times f_{n\ell}(0) = 0, \quad (\text{A15})$$

$$u_{n\ell}(r_{N+1}) = r_{N+1} f_{n\ell}(r_{N+1}) = r_{N+1} \times 0 = 0. \quad (\text{A16})$$

Here, $u_{n\ell}(r_0)$ vanishes by definition of $u_{n\ell}$, while $u_{n\ell}(r_{N+1})$ is zero to ensure that the wavefunction $f_{n\ell}$ vanishes at the box edge. For the second derivative in equation (A12), we discretize as follows:

$$\begin{aligned} \frac{d^2 u}{dr^2} &= \frac{d}{dr} \left(\frac{du}{dr} \right) \\ &:= \lim_{\Delta r \rightarrow 0} \frac{\frac{[u(r+2\Delta r) - u(r+\Delta r)]}{\Delta r} - \frac{[u(r+\Delta r) - u(r)]}{\Delta r}}{\Delta r} \\ &= \lim_{\Delta r \rightarrow 0} \frac{u(r) - 2u(r+\Delta r) + u(r+2\Delta r)}{\Delta r^2} \\ &\xrightarrow{r \rightarrow r_{i-1}} \frac{u(r_{i-1}) - 2u(r_i) + u(r_{i+1}))}{\Delta r^2} \end{aligned} \quad (\text{A17})$$

This converts equation (A6) into a coupled set of $N+2$ linear equations.

$$\left(\chi_\ell(r_i) u_{n\ell}(r_i) - \frac{u(r_{i-1}) - 2u(r_i) + u(r_{i+1}))}{\Delta r^2} \right) = 2E_{n\ell} u_{n\ell}(r_i), \quad (\text{A18})$$

where $i \in \{0, 1, 2, \dots, N, N+1\}$. The equations for r_0 and r_{N+1} are fixed by the boundary conditions (A15) and (A16), leaving N independent equations

$$0.5 \left(\begin{bmatrix} \chi_\ell(r_1) & 0 & 0 & \dots & 0 \\ 0 & \chi_\ell(r_2) & 0 & \dots & 0 \\ \vdots & \ddots & \ddots & \ddots & 0 \\ \vdots & \ddots & \ddots & \chi_\ell(r_{N-1}) & 0 \\ 0 & \dots & \dots & 0 & \chi_\ell(r_N) \end{bmatrix} - \frac{1}{\Delta r^2} \begin{bmatrix} -2 & 1 & 0 & \dots & 0 \\ 1 & -2 & 1 & \dots & 0 \\ \vdots & \ddots & \ddots & \ddots & 0 \\ \vdots & \ddots & 1 & -2 & 1 \\ 0 & \dots & \dots & 1 & -2 \end{bmatrix} \right) \begin{bmatrix} u_{n\ell}(r_1) \\ u_{n\ell}(r_2) \\ u_{n\ell}(r_3) \\ \vdots \\ u_{n\ell}(r_{N-1}) \\ u_{n\ell}(r_N) \end{bmatrix} = E_{n\ell} \begin{bmatrix} u_{n\ell}(r_1) \\ u_{n\ell}(r_2) \\ u_{n\ell}(r_3) \\ \vdots \\ u_{n\ell}(r_{N-1}) \\ u_{n\ell}(r_N) \end{bmatrix}. \quad (\text{A19})$$

This is now a standard matrix eigenvalue problem, with eigenvectors $u_{n\ell}$ and eigenvalues $E_{n\ell}$

$$A_l u_{n\ell} = E_{n\ell} u_{n\ell}, \quad (\text{A20})$$

where A_l is a real, symmetric $N \times N$ matrix. We ordering the eigenvalues $E_{0\ell}, \dots, E_{N-1,\ell}$ from smallest to largest. The eigenvectors $u_{n\ell}$ are related to the original radial eigenfunctions via $f_{n\ell}(r) = u_{n\ell}(r)/r$, so

$$\psi_{n\ell m}(\mathbf{r}) = f_{n\ell}(r) Y_{\ell m}(\theta, \phi). \quad (\text{A21})$$

A potential source of confusion is to conflate the continuum limit of the *discretization* with the *free-space* limit of the underlying eigenvalue problem. Refining the grid ($N \rightarrow \infty$ at fixed r_{\max}) does not introduce a missing continuous sector: it simply yields a more accurate representation of the same eigenvalue problem posed on a finite interval with the boundary conditions adopted here. For fixed ℓ and fixed r_{\max} , Eq. (12) is a regular self-adjoint Sturm–Liouville problem on $[0, r_{\max}]$, and therefore has a purely discrete spectrum with a complete orthonormal

set of radial eigenfunctions $u_{n\ell}(r)$; correspondingly, the resolution of the identity in Eq. (14) is purely discrete in this setting. A continuous contribution (schematically $\int d\lambda |\lambda\rangle\langle\lambda|$) becomes relevant only in the free-space limit $r_{\max} \rightarrow \infty$, where the spectral structure changes.

Appendix B: Orbital resonance of black holes

1. Lagrangian for the Black Hole

We treat the black hole as a classical point particle of mass M moving in two-dimensional polar coordinates (r, ϕ) and confine its motion to the equatorial plane ($\theta = \pi/2$) throughout. In polar coordinates, the position is

$$\mathbf{X}(t) = r(t) \hat{e}_r(\phi(t)). \quad (\text{B1})$$

and the kinetic energy is then the usual sum of radial and azimuthal contributions,

$$T = \frac{1}{2} M_{BH} (\dot{r}^2 + r^2 \dot{\phi}^2). \quad (\text{B2})$$

The potential energy is decomposed into a spherically symmetric ULDM ground-state potential plus a perturbation associated with a given excited mode:

$$V = M\Phi_U(r, \phi, t) = M[\Phi_0(r) + \delta\Phi_U(\mathbf{r}, t)]. \quad (\text{B3})$$

Critically, the perturbation also modifies the gravitational potential. Given equation A21 we can write a time-dependent wavefunction as a linear superposition,

$$\Psi(r, \theta, \phi, t) = \sum_{n\ell m} c_{n\ell m}(t) \psi_{n\ell m}(r, \theta, \phi), \quad (\text{B4})$$

where the coefficients $c_{n\ell m}(t)$ encode the time dependence. The ground-state soliton corresponds to the mode with $n = \ell = m = 0$,

$$\Psi_0(r) = f_{00}(r) Y_{00}, \quad (\text{B5})$$

and add a single mode with amplitude ϵ :

$$\begin{aligned} \Psi(\mathbf{r}, t) &= \Psi_0 + \epsilon \cdot \delta\Psi^{n\ell m}(\mathbf{r}, t), \\ \delta\Psi^{n\ell m}(\mathbf{r}, t) &= c_{n\ell m}(t) f_{n\ell}(r) Y_{\ell m}(\theta, \phi). \end{aligned} \quad (\text{B6})$$

We excite a single dipole modes with $\ell = 1$:

$$\delta\Psi^{n1m}(\mathbf{r}, t) = c_{n1m}(t) f_{n1}(r) Y_{1m}(\theta, \phi). \quad (\text{B7})$$

In principle one could examine the coupling between the soliton eigenmodes and an orbiting mass but we will inject the empirical time dependence of $c_{n1m}(t)$ we found from numerical simulations (see Figure 9), or

$$\begin{aligned} c_{n1m}(t) &\approx C \cos(\omega_{dip}t) e^{i\bar{\omega}t}, \\ \bar{\omega} &= \frac{\omega_1 + \omega_2}{2}, \\ \omega_{dip} &= \frac{\omega_2 - \omega_1}{2}, \end{aligned} \quad (\text{B8})$$

where C is a complex constant and ω_{dip} is the eigenfrequency of the mode. Consequently, we have

$$\delta\Psi \approx C\epsilon \cos(\omega_{dip}t) e^{i\bar{\omega}t} f_{n1}(r) Y_{1m}(\theta, \phi) \quad (\text{B9})$$

The ULDM density is given by

$$\rho(\mathbf{r}, t) = |\Psi(r, t)|^2. \quad (\text{B10})$$

Substituting $\Psi(\mathbf{r}, t) = \Psi_0 + \delta\Psi$ and linearizing yields

$$|\Psi_0 + \delta\Psi|^2 = |\Psi_0|^2 + \Psi_0\delta\Psi^* + \Psi_0^*\delta\Psi + \mathcal{O}(|\delta\Psi|^2). \quad (\text{B11})$$

Thus, the density perturbation can be written as

$$\delta\rho = \Psi_0^*\delta\Psi + \Psi_0\delta\Psi^* = 2\Re[\Psi_0^*\delta\Psi]. \quad (\text{B12})$$

Substituting (B9), we find:

$$\begin{aligned} \delta\rho &= 2\Re[\Psi_0^*C \cos(\omega_{dip}t)\epsilon e^{i\bar{\omega}t} f_{n1}(r) Y_{1m}(\theta, \phi)] \\ &= 2|C||\epsilon| \Psi_0 f_{n1}(r) \Re[e^{i\alpha} e^{i\bar{\omega}t} Y_{1m}(\theta, \phi)], \end{aligned} \quad (\text{B13})$$

where the ground-state wavefunction Ψ_0 and the radial part $f_{n1}(r)$ of the excited mode are both taken to be real and α is defined as the phase of the product $C\epsilon$. Since we restrict to equatorial-plane motion ($\theta = \pi/2$) $Y_{1m}(\theta, \phi)$ reduces to

$$Y_{1m}\left(\frac{\pi}{2}, \phi\right) = \begin{cases} \sqrt{\frac{3}{8\pi}} e^{-i\phi}, & m = -1, \\ 0, & m = 0, \\ \sqrt{\frac{3}{8\pi}} e^{+i\phi}, & m = +1, \end{cases} \quad (\text{B14})$$

and density perturbation becomes

$$\delta\rho = 2|C||\epsilon| \Psi_0 f_{n1}(r) \begin{cases} \sqrt{\frac{3}{8\pi}} \Re\{e^{i(\alpha-\phi+\bar{\omega}t)}\}, & m = -1, \\ 0, & m = 0, \\ \sqrt{\frac{3}{8\pi}} \Re\{e^{i(\alpha+\phi+\bar{\omega}t)}\}, & m = +1. \end{cases} \quad (\text{B15})$$

A corollary of this choice is that the $m = 0$ dipole modes is not relevant to the stone skipping. Given rotational symmetry we absorb $\alpha \pm \phi$ into α by a redefinition of the azimuthal origin and write

$$\delta\rho_{\pm} = 2|C||\epsilon| f_{00}(r) f_{n1}(r) \cos(\omega_{dip}t) \cos(\phi \pm \bar{\omega}t), \quad (\text{B16})$$

where the subscript plus and minus signs correspond respectively to $m = +1$ and $m = -1$.

The next step is to use the Poisson equation

$$\nabla^2 \delta\Phi = 4\pi G \delta\rho, \quad (\text{B17})$$

to convert $\delta\rho_{\pm}$ into a gravitational potential perturbation $\delta\Phi$. Again expanding in spherical harmonics

$$\delta\rho = \sum_{\ell, m} \rho_{\ell m} Y_{\ell m}, \quad \delta\Phi = \sum_{\ell, m} \Phi_{\ell m} Y_{\ell m} \quad (\text{B18})$$

and substituting into Eq. (B16) orthogonality shows each (ℓ, m) mode satisfies its own radial differential equation,

$$\frac{1}{r^2} \frac{d}{dr} \left(r^2 \frac{d\Phi_{\ell m}}{dr} \right) - \frac{\ell(\ell+1)}{r^2} \Phi_{\ell m} = 4\pi G \rho_{\ell m}. \quad (\text{B19})$$

Our focus is $(\ell, m) = (1, m)$ and it is convenient to write

$$\delta\Phi = \epsilon_{\Phi} \Phi_{1m} \cos(\omega_{dip}t) \cos(\phi \pm \bar{\omega}t), \quad (\text{B20})$$

where ϵ_{Φ} absorbs all constant prefactors; for brevity we write ϵ in what follows.

The full Lagrangian for a black hole moving in a ULDM soliton with an $\ell = 1$ dipole perturbation is

$$\begin{aligned} L &= \frac{1}{2} M_{BH} (\dot{r}^2 + r^2 \dot{\phi}^2) \\ &\quad - M_{BH} [\Phi_0(r) + \epsilon \Phi_{1m}(r) \cos(\omega_{dip}t) \cos(\phi - \bar{\omega}t)]. \end{aligned} \quad (\text{B21})$$

In Eq. (B21) we choose the combination $\phi - \bar{\omega}t$, corresponding to the $m = -1$ mode.

Given the presence of non-conservative drag forces Q_i ,

$$\frac{d}{dt} \frac{\partial \mathcal{L}}{\partial \dot{q}_i} - \frac{\partial \mathcal{L}}{\partial q_i} = Q_i. \quad (\text{B22})$$

In planar polar coordinates $\mathbf{f} = f_r \hat{\mathbf{e}}_r + f_\phi \hat{\mathbf{e}}_\phi$, so that $Q_r = F_r$ and $Q_\phi = rF_\phi$. The equations of motion are thus

$$\ddot{r} - r\dot{\phi}^2 + \frac{d\Phi_0(r)}{dr} + \epsilon \frac{d\Phi_{1m}(r)}{dr} \cos(\omega_{dip}t) \cos(\phi - \bar{\omega}t) = \frac{Q_r}{M_{BH}}, \quad (\text{B23})$$

$$\frac{d}{dt} (r^2 \dot{\phi}) - \epsilon \Phi_{1m}(r) \cos(\omega_{dip}t) \sin(\phi - \bar{\omega}t) = \frac{Q_\phi}{M_{BH}}. \quad (\text{B24})$$

For tractability we assume that the frictional force is proportional to the velocity,

$$\begin{aligned} f_r &= -M_{BH} \gamma_r \dot{r}, \\ f_\phi &= -M_{BH} \gamma_\phi r \dot{\phi}, \end{aligned} \quad (\text{B25})$$

introduce damping coefficients γ_r and γ_ϕ . Taking the above expressions and equations (B25) and (7),

$$\gamma_{r,\phi} = A \frac{4\pi\rho(r,t) G^2 M_{BH} m^2 r^2}{3\hbar^2 \sqrt{\dot{r}^2 + r^2 \dot{\phi}^2}}. \quad (\text{B26})$$

the generalized forces become

$$\begin{aligned} Q_r &= -M_{BH} \gamma_r \dot{r}, \\ Q_\phi &= -M_{BH} \gamma_\phi r^2 \dot{\phi}. \end{aligned} \quad (\text{B27})$$

As a starting point it is useful to consider the simplest limit: an unperturbed circular orbit with no excitation and no dynamical friction, *i.e.* $\Phi = 0$ and $\gamma_r = \gamma_\phi = 0$, which gives

$$\ddot{r} - r\dot{\phi}^2 + \frac{d\Phi_0(r)}{dr} = 0, \quad \frac{d}{dt} (r^2 \dot{\phi}) = 0. \quad (\text{B28})$$

To restrict to circular orbits we set $r(t) = r_0$ and $\dot{r} = 0$, and write $\phi(t) = \Omega_0 t + \phi_0$. The radial part of Eq. (B28) then yields the circular-orbit potential–frequency relation

$$r_0 \Omega_0^2 = \Phi'_0(r_0). \quad (\text{B29})$$

The azimuthal equation reproduces the usual conservation of angular momentum and will not be needed.

2. Linearised quasi-circular expansion

Once we include dynamical friction the orbits become quasi-circular. We write the perturbation as

$$r(t) = r_0 + \xi(t), \quad \phi(t) = \Omega_0 t + \eta(t), \quad (\text{B30})$$

where the perturbations ξ, η are first order, or $|\xi| \ll r_0$ and $|\eta| \ll 1$. Under these assumptions we expand

$r\dot{\phi}^2$, the derivative of the spherically symmetric potential $\Phi'_0(r)$, and the dipole term $\epsilon \Phi'_{1m}(r) \cos(\phi + \omega_{dip}t)$ about the circular orbit. Introducing constants

$$C_r = \Phi'_{1m}(r_0), \quad C_\phi = \Phi_{1m}(r_0), \quad (\text{B31})$$

to encode the radial profiles of the dipole perturbation, the linearized expansions are

$$r\dot{\phi}^2 \simeq r_0 \Omega_0^2 + \Omega_0^2 \xi + 2r_0 \Omega_0 \dot{\eta}, \quad (\text{B32a})$$

$$\Phi'_0(r) \simeq \Phi'_0(r_0) + \xi \Phi''_0(r_0), \quad (\text{B32b})$$

$$\Phi'_{1m}(r) \simeq \Phi'_{1m}(r_0) + \xi \Phi''_{1m}(r_0), \quad (\text{B32c})$$

$$\cos(\phi - \bar{\omega}t) \simeq \cos((\Omega_0 - \bar{\omega})t) - \eta \sin((\Omega_0 - \bar{\omega})t). \quad (\text{B32d})$$

and, up to $\mathcal{O}(\epsilon^2)$,

$$\frac{d}{dt} (r^2 \dot{\phi}) \simeq r_0^2 \dot{\eta} + 2r_0 \Omega_0 \dot{\xi}, \quad (\text{B33a})$$

$$r^2 \dot{\phi}^2 \simeq -r_0^2 (\Omega_0 + \dot{\eta}) - 2\Omega_0 r_0 \xi, \quad (\text{B33b})$$

$$\epsilon \Phi'_{1m}(r) \cos(\phi - \bar{\omega}t) \simeq \epsilon C_r \cos((\Omega_0 - \bar{\omega})t), \quad (\text{B33c})$$

$$\epsilon \Phi'_{1m}(r) \sin(\phi + \omega t) \simeq \epsilon C_\phi \sin((\Omega_0 + \omega)t). \quad (\text{B33d})$$

Substituting Eqs. (B31)–(B33d) into the equations of motion and using the circular-orbit identity (B29), we obtain the coupled linear system

$$\begin{cases} \ddot{\xi} + \mathcal{A} \xi - 2r_0 \Omega_0 \dot{\eta} + \gamma_r \dot{\xi} = F_r(t), \\ r_0^2 \ddot{\eta} + 2r_0 \Omega_0 \dot{\xi} + \gamma_\phi r_0^2 (\Omega_0 + \dot{\eta}) = F_\phi(t), \end{cases} \quad (\text{B34})$$

where for convenience we defined

$$\begin{aligned} F_r(t) &\equiv -0.5\epsilon C_r [\cos(\omega_1 t - \Omega_0) + \cos(\omega_2 t + \Omega_0)], \\ F_\phi(t) &\equiv -0.5\epsilon C_\phi [\sin(\omega_1 t - \Omega_0) + \sin(\omega_2 t + \Omega_0)], \\ \mathcal{A} &\equiv V''_0(r_0) - \Omega_0^2. \end{aligned} \quad (\text{B35})$$

Equation (B34) is a coupled linear system for $\xi(t)$ and $\eta(t)$. We first examine the case with no driving or damping, *i.e.* $\epsilon = \gamma_r = \gamma_\phi = 0$. In this limit Eq. (B34) reduces to the homogeneous system

$$\begin{cases} \ddot{\xi} + \mathcal{A} \xi - 2r_0 \Omega_0 \dot{\eta} = 0, \\ r_0^2 \ddot{\eta} + 2r_0 \Omega_0 \dot{\xi} = 0. \end{cases} \quad (\text{B36})$$

Differentiating the first of these equations with respect to time and using the second to eliminate $\ddot{\eta}$ gives

$$\ddot{\xi} + \mathcal{A}\dot{\xi} + 4\Omega_0^2 \xi = 0. \quad (\text{B37})$$

Defining $u(t) \equiv \dot{\xi}(t)$,

$$\ddot{u} + \kappa^2 u = 0, \quad (\text{B38})$$

with intrinsic frequency

$$\kappa^2 = \mathcal{A} + 4\Omega_0^2 = \Phi_0''(r_0) + 3\Omega_0^2. \quad (\text{B39})$$

Thus, in the absence of dynamical friction and excitation, the soliton–black-hole system exhibits small oscillations around the circular orbit with natural frequency κ .

Next we turn to the case with driving but no damping ($\epsilon \neq 0, \gamma_r = \gamma_\phi = 0$). In this regime Eq. (B34) reduces to

$$\begin{cases} \ddot{\xi} + \mathcal{A}\dot{\xi} - 2r_0\Omega_0\dot{\eta} = F_r(t), \\ r_0^2\ddot{\eta} + 2r_0\Omega_0\dot{\xi} = F_\phi(t). \end{cases} \quad (\text{B40})$$

Differentiating the first equation yields

$$\ddot{\xi} + \mathcal{A}\dot{\xi} - 2r_0\Omega_0\dot{\eta} = \dot{F}_r(t), \quad (\text{B41})$$

where $\dot{F}_r(t)$ is the time derivative of $F_r(t)$. Solving the second equation of Eq. (B40) for $\dot{\eta}$, we find

$$\dot{\eta} = \frac{1}{r_0^2} [F_\phi(t) - 2r_0\Omega_0\dot{\xi}]. \quad (\text{B42})$$

Substituting Eq. (B42) into Eq. (B41) and using $\kappa^2 = \mathcal{A} + 4\Omega_0^2$ gives

$$\ddot{\xi} + \kappa^2 \dot{\xi} = \dot{F}_r(t) + \frac{2\Omega_0}{r_0} F_\phi(t). \quad (\text{B43})$$

This gives the forced harmonic oscillator

$$\ddot{u} + \kappa^2 u = F(t), \quad (\text{B44})$$

driven by a single-frequency forcing term

$$\begin{aligned} F(t) &= \dot{F}_r(t) + \frac{2\Omega_0}{r_0} F_\phi(t) \\ &= F_1 \sin(\omega_1 t - \Omega_0) + F_2 \sin(\omega_2 t + \Omega_0), \\ F_{1,2} &= a\omega_{1,2} + b, \\ a &= \frac{C_r \epsilon}{2}, b = -\frac{\Omega_0 C_\phi \epsilon}{r_0}, \end{aligned} \quad (\text{B45})$$

The resonance condition is simply

$$\kappa = \omega_{1,2}, F_{1,2} \neq 0, \quad (\text{B46})$$

and combining Eqs. (B39) and (B46) yields the dipole frequency required for resonance,

$$\omega_R = \omega_{1,2} = \Phi_0''(r_0) + 3\Omega_0^2. \quad (\text{B47})$$

We now add the damping and in this situation Eq. (B34) is our equation of motion. As before, we differentiate the radial equation to obtain

$$\ddot{\xi} + \mathcal{A}\dot{\xi} - 2r_0\Omega_0\dot{\eta} + \gamma_r \ddot{\xi} = \dot{F}_r(t), \quad (\text{B48})$$

and use the azimuthal equation to express $\dot{\eta}$ in terms of $\xi, \dot{\xi}$ and the effective azimuthal driving term,

$$\dot{\eta} = \frac{1}{r_0^2} \left[F_\phi(t) - 2r_0\Omega_0\dot{\xi} - \gamma_\phi r_0^2 (\Omega_0 + \dot{\eta}) - 2\gamma_\phi \Omega_0 r_0 \xi \right]. \quad (\text{B49})$$

Combining these results leads to

$$\begin{aligned} \dot{F}_r(t) + \frac{2\Omega_0}{r_0} F_\phi(t) &= \ddot{\xi} + \kappa^2 \dot{\xi} + 2\gamma_\phi r_0 \Omega_0^2 \\ &\quad + 2\gamma_\phi r_0 \Omega_0 \dot{\eta} + 4\Omega_0^2 \gamma_\phi \xi + \gamma_r \ddot{\xi}, \end{aligned} \quad (\text{B50})$$

which still contains $\dot{\eta}$. To eliminate $\dot{\eta}$ we use the radial equation (B34) once more to rewrite

$$2r_0\Omega_0\dot{\eta} = \ddot{\xi} + \mathcal{A}\dot{\xi} + \gamma_r \dot{\xi} - F_r(t). \quad (\text{B51})$$

Substituting this back yields the third-order equation

$$\ddot{\xi} + (\gamma_\phi + \gamma_r) \dot{\xi} + (\kappa^2 + \gamma_\phi \gamma_r) \dot{\xi} + \gamma_\phi \kappa^2 \xi = G(t), \quad (\text{B52})$$

where the effective driving term is

$$G(t) \equiv \dot{F}_r(t) + \gamma_\phi F_r(t) + \frac{2\Omega_0}{r_0} F_\phi(t) - 2\gamma_\phi r_0 \Omega_0^2. \quad (\text{B53})$$

3. Forced damped harmonic oscillator

Eq. (B52) contains a term proportional to ξ in addition to derivatives up to third order, it cannot, in general, be cast into the standard form of a forced damped harmonic oscillator equation for $u = \dot{\xi}$,

$$\ddot{u} + 2\Gamma \dot{u} + \kappa^2 u = F(t). \quad (\text{B54})$$

On closer inspection, the situation simplifies considerably if we keep $\gamma_r \neq 0$ but set $\gamma_\phi = 0$. Physically, $\gamma_\phi = 0$ corresponds to switching off azimuthal damping, which mainly controls the secular decay of the orbital angular momentum. The ‘‘resonant amplification of the radial amplitude’’ that we are interested in is essentially a local process, occurring on a timescale short compared with the orbital decay time. Treating Ω_0 as approximately constant, Eq. (B52) reduces to Eq. (B54), where

$$\Gamma = \frac{1}{2} \gamma_r, \quad \kappa^2 = \Phi_0''(r_0) + 3\Omega_0^2, \quad (\text{B55})$$

and the driving term is

$$\begin{aligned} F_1(t) &= (a\omega_1 + b) \sin(\omega_1 t - \Omega_0), \\ F_2(t) &= (a\omega_2 + b) \sin(\omega_2 t + \Omega_0). \end{aligned} \quad (\text{B56})$$

To extract the intrinsic frequency in the damped case, it is convenient to consider the complex form

$$\ddot{u} + 2\Gamma \dot{u} + \kappa^2 u = \text{Im}[F(\omega) e^{i\omega t}], \quad (\text{B57})$$

and assume a steady-state particular solution

$$u(\omega) = \text{Im}[U(\omega) e^{i\omega t}]. \quad (\text{B58})$$

Neglecting the homogeneous solution (which decays on the timescale set by Γ), substitution into Eq. (B57) yields the complex amplitude

$$U(\omega) = \frac{F(\omega)}{\kappa^2 - \omega^2 + 2i\Gamma\omega}. \quad (\text{B59})$$

The corresponding physical solution for $u(t)$ is

$$\begin{aligned} u(\omega) &= \mathcal{U}(\omega) \sin(\omega t + \delta), \\ \mathcal{U}(\omega) &= \frac{a\omega + b}{\sqrt{(\kappa^2 - \omega^2)^2 + (2\Gamma\omega)^2}}, \\ \delta &= \arctan \frac{-2\Gamma\omega}{\kappa^2 - \omega^2}. \end{aligned} \quad (\text{B60})$$

The resonance condition occurs where the derivation of the non-oscillatory part $\mathcal{U}(\omega)$ for the maximum value occurs. The story is not quite complete, however: $u = \dot{\xi}$, and we are interested in resonance of the orbital radius itself, not of its derivative. To address this we define

$$\xi(\omega) = \text{Im}[\Xi(\omega) e^{i\omega t}], \quad (\text{B61})$$

which implies

$$\dot{\xi} = \text{Im}[\Xi(\omega) i\omega e^{i\omega t}] = u, \quad (\text{B62})$$

so that

$$\Xi(\omega) = -\frac{iU(\omega)}{\omega} = -\frac{iF(\omega)}{\omega(\kappa^2 - \omega^2 + 2i\Gamma\omega)}. \quad (\text{B63})$$

From this it follows that

$$\begin{aligned} \xi(\omega) &= \mathcal{X}(\omega) \sin(\omega t + \delta - \frac{\pi}{2}), \\ \mathcal{X}(\omega) &= \frac{a\omega + b}{\omega \sqrt{(\kappa^2 - \omega^2)^2 + (2\Gamma\omega)^2}}. \end{aligned} \quad (\text{B64})$$

If there exists an $\omega = \omega_{\max}$ such that

$$\left. \frac{d\mathcal{X}}{d\omega} \right|_{\omega_{\max}} = 0, \quad \left. \frac{d^2\mathcal{X}}{d\omega^2} \right|_{\omega_{\max}} < 0, \quad (\text{B65})$$

then the resonance condition is determined by

$$\omega_R = \omega_{\max}. \quad (\text{B66})$$

For the full expression of \mathcal{X} , a closed-form solution for ω_{\max} does not generally exist. However, if the system satisfies

$$\omega \gg -\frac{2\Omega_0\Phi_{1m}(r_0)}{r_0\Phi'_{1m}(r_0)} = \frac{b}{a} > 0, \quad (\text{B67})$$

we may approximate

$$\mathcal{X}(\omega) \approx \mathcal{X}_a(\omega) = \frac{a}{\sqrt{(\kappa^2 - \omega^2)^2 + (2\Gamma\omega)^2}}. \quad (\text{B68})$$

This is the standard forced, damped oscillator response, for which resonance occurs at

$$\omega_R = \sqrt{\kappa^2 - 2\Gamma^2}, \quad \frac{\Gamma}{\kappa} < \frac{1}{\sqrt{2}}. \quad (\text{B69})$$

In the opposite limit, if

$$0 < \omega \ll -\frac{2\Omega_0\Phi_{1m}(r_0)}{r_0\Phi'_{1m}(r_0)}, \quad (\text{B70})$$

we may instead approximate

$$\mathcal{X}(\omega) \approx \mathcal{X}_b(\omega) = \frac{b}{\omega \sqrt{(\kappa^2 - \omega^2)^2 + (2\Gamma\omega)^2}}. \quad (\text{B71})$$

We define a new denominator function controlling the radial amplitude,

$$D_1(\omega) \equiv \omega^2 [(\kappa^2 - \omega^2)^2 + (2\Gamma\omega)^2]. \quad (\text{B72})$$

Differentiating, we find

$$\frac{dD_1(\omega)}{d\omega} = 6\omega \left[\omega^4 + \frac{4}{3}(2\Gamma^2 - \kappa^2)\omega^2 + \frac{\kappa^4}{3} \right]. \quad (\text{B73})$$

If the quartic polynomial inside the brackets is non-negative for all ω , then $D_1(\omega)$ attains its minimum at $\omega = 0$, and $\xi(\omega)$ would diverge there with no finite maximum at nonzero ω . To obtain a genuine resonance at a non-zero frequency we therefore require that this quartic be negative over some interval in ω , which is equivalent to demanding that the discriminant

$$\Delta = \frac{16(2\Gamma^2 - \kappa^2)^2}{9} - \frac{4\kappa^4}{3} = \frac{4(\kappa^2 - 8\Gamma^2)^2 - 48\Gamma^4}{9} \geq 0, \quad (\text{B74})$$

or, in terms of the ratio $x^2 = \Gamma^2/\kappa^2$,

$$\frac{\kappa^2}{\Gamma^2} \in \left[0, \frac{1}{8 + 4\sqrt{3}} \right] \cup \left[\frac{1}{8 - 4\sqrt{3}}, \infty \right]. \quad (\text{B75})$$

Within these ranges, the condition $dD_1(\omega)/d\omega = 0$ admits three solutions for $\mu = \omega^2$:

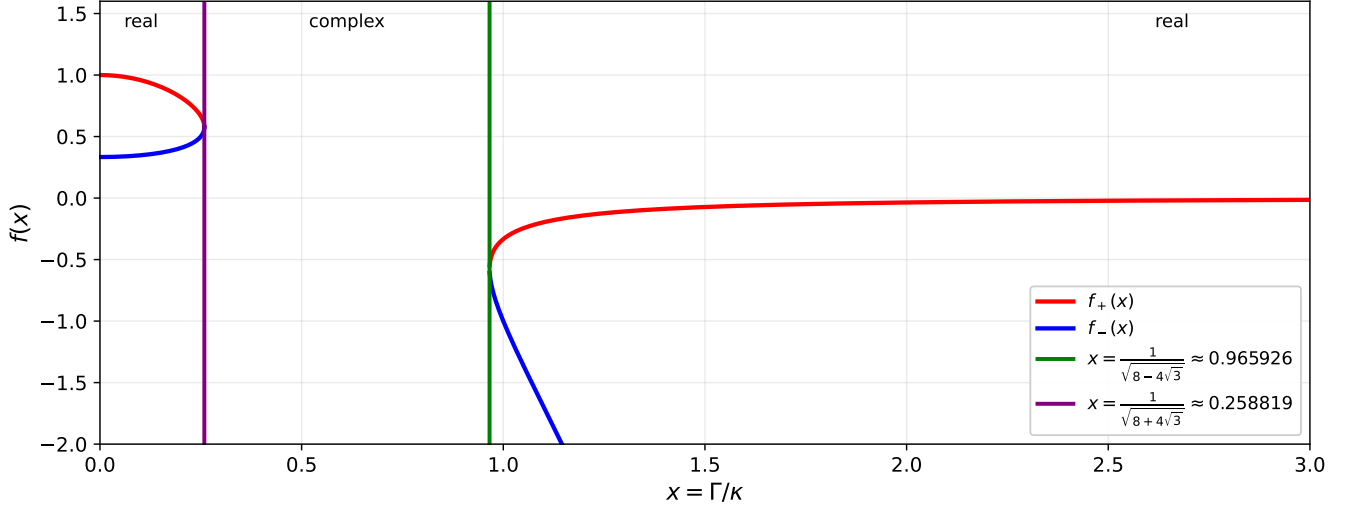
$$\mu_0 = 0, \quad \mu_{\pm} = \frac{2\kappa^2 - 4\Gamma^2 \pm \sqrt{\kappa^4 - 16\kappa^2\Gamma^2 + 16\Gamma^4}}{3}. \quad (\text{B76})$$

The two nonzero solutions can be written in the rescaled form

$$\frac{\mu_{\pm}^2}{\kappa^2} = \frac{1}{3} \left[2 - 4\left(\frac{\Gamma}{\kappa}\right)^2 \pm 4\sqrt{\left(\frac{\Gamma}{\kappa}\right)^2 - \frac{1}{2}} \right] - \frac{3}{16}, \quad (\text{B77})$$

and defining the auxiliary function

$$f_{\pm}(x) = \frac{1}{3} \left[2 - 4x^2 \pm 4\sqrt{(x^2 - \frac{1}{2})^2} \right] - \frac{3}{16}, \quad (\text{B78})$$

FIG. 10. The auxiliary function $f(x)$

one finds that in Figure 10 for $x^2 = \Gamma^2/\kappa^2 \in [\frac{1}{8-4\sqrt{3}}, \infty]$ the three roots satisfy $0 = \mu_0 > \mu_+ > \mu_-$, and $D_1(\omega)$ again attains its minimum at μ_0 , so $\xi(\omega)$ diverges at $\omega = 0$ and has no maximum. For $x^2 = \Gamma^2/\kappa^2 \in [0, \frac{1}{8+4\sqrt{3}}]$, however, one finds $\mu_1 > \mu_2 > \mu_0 = 0$, and $D_1'(\omega)$ is monotonically increasing on the interval $[\mu_0, \mu_2]$ and $[\mu_1, \infty]$.

Since $\mu_0 = 0$ corresponds to a singular point, we dis-

card it, leaving a unique resonance at

$$\omega_d^2 = \mu_2 = \frac{\kappa^2}{3} \left[2 - 4 \left(\frac{\Gamma}{\kappa} \right)^2 + 4 \sqrt{\left(\frac{\Gamma}{\kappa} \right)^2 - \frac{1}{2}} \right] - \frac{3}{16}, \quad (\text{B79})$$

which in the small-damping regime $\Gamma/\kappa \ll 1$ reduces to

$$\omega_d^2 \simeq \kappa^2 - 4\Gamma^2. \quad (\text{B80})$$

So, the resonance of the radial amplitude $\xi(\omega)$ occurs when the driving frequency satisfies

$$\omega_d^2 = \begin{cases} \frac{\kappa^2}{3} \left[2 - 4 \left(\frac{\Gamma}{\kappa} \right)^2 + 4 \sqrt{\left(\frac{\Gamma}{\kappa} \right)^2 - \frac{1}{2}} \right] - \frac{3}{16}, & \frac{\Gamma}{\kappa} < \frac{1}{8+4\sqrt{3}}, \\ \kappa^2 - 2\Gamma^2, & \frac{\Gamma}{\kappa} < \frac{1}{\sqrt{2}}, \end{cases} \quad \begin{cases} 0 < \omega \ll -\frac{2\Omega_0\Phi_{1m}(r_0)}{r_0\Phi'_{1m}(r_0)}, \\ \omega \gg -\frac{2\Omega_0\Phi_{1m}(r_0)}{r_0\Phi'_{1m}(r_0)} > 0 \end{cases} \quad (\text{B81})$$

- [1] Planck Collaboration, N. Aghanim, *et al.*, *Astron. Astrophys.* **641**, A6 (2020).
- [2] V. Springel *et al.*, *Nature* **435**, 629 (2005).
- [3] C. S. Frenk and S. D. M. White, *Annalen Phys.* **524**, 507 (2012).
- [4] J. R. Primack, *Annalen Phys.* **524**, 535 (2012).
- [5] B. Moore, *Nature* **370**, 629 (1994).
- [6] W. J. G. de Blok, *Adv. Astron.* **2010**, 789293 (2010).
- [7] S.-H. Oh *et al.*, *Astron. J.* **141**, 193 (2011).
- [8] J. S. Bullock and M. Boylan-Kolchin, *Annu. Rev. Astron. Astrophys.* **55**, 343 (2017).
- [9] D. H. Weinberg, J. S. Bullock, F. Governato, R. Kuzio de Naray, and A. H. G. Peter, *Proc. Natl. Acad. Sci. U.S.A.* **112**, 12249 (2015).
- [10] M. Boylan-Kolchin, J. S. Bullock, and M. Kaplinghat, *Mon. Not. R. Astron. Soc.* **415**, L40 (2011).
- [11] D. N. Spergel and P. J. Steinhardt, *Phys. Rev. Lett.* **84**, 3760 (2000).
- [12] J. L. Feng, *Annu. Rev. Astron. Astrophys.* **48**, 495 (2010).
- [13] G. Bertone, D. Hooper, and J. Silk, *Phys. Rep.* **405**, 279 (2005).
- [14] W. Hu, R. Barkana, and A. Gruzinov, *Phys. Rev. Lett.* **85**, 1158 (2000).
- [15] D. J. E. Marsh, *Phys. Rep.* **643**, 1 (2016).
- [16] L. Hui, J. P. Ostriker, S. Tremaine, and E. Witten, *Phys. Rev. D* **95**, 043541 (2017).
- [17] E. G. M. Ferreira, *Astron. Astrophys. Rev.* **29**, 7 (2021).
- [18] A. Eberhardt and E. G. M. Ferreira, *Ultralight fuzzy dark matter review (2025)*, arXiv:2507.00705 [astro-ph.CO].

- [19] A. Arvanitaki, S. Dimopoulos, S. Dubovsky, N. Kaloper, and J. March-Russell, *Phys. Rev. D* **81**, 123530 (2010).
- [20] P. Svrcek and E. Witten, *J. High Energy Phys.* **06** (06), 051.
- [21] E. Witten, *Phys. Lett. B* **149**, 351 (1984).
- [22] L. M. Widrow and N. Kaiser, *Astrophys. J. Lett.* **416**, L71 (1993).
- [23] P.-H. Chavanis, *Phys. Rev. D* **84**, 043531 (2011).
- [24] H.-Y. Schive, T. Chiueh, and T. Broadhurst, *Nat. Phys.* **10**, 496 (2014), arXiv:1406.6586 [astro-ph.GA].
- [25] H.-Y. Schive, M.-H. Liao, T.-P. Woo, S.-K. Wong, T. Chiueh, T. Broadhurst, and W.-Y. P. Hwang, *Phys. Rev. Lett.* **113**, 261302 (2014).
- [26] P. Mocz *et al.*, *Mon. Not. R. Astron. Soc.* **471**, 4559 (2017).
- [27] B. Schwabe, J. C. Niemeyer, and J. F. Engels, *Phys. Rev. D* **94**, 043513 (2016).
- [28] J. Veltmaat, J. C. Niemeyer, and B. Schwabe, *Phys. Rev. D* **98**, 043509 (2018).
- [29] S.-C. Lin, H.-Y. Schive, S.-K. Wong, and T. Chiueh, *Phys. Rev. D* **97**, 063523 (2018).
- [30] V. Iršič *et al.*, *Phys. Rev. Lett.* **119**, 031302 (2017).
- [31] K. K. Rogers and H. V. Peiris, *Phys. Rev. Lett.* **126**, 071302 (2021).
- [32] E. Armengaud *et al.*, *Mon. Not. R. Astron. Soc.* **471**, 4606 (2017).
- [33] N. Dalal and A. Kravtsov, *Phys. Rev. D* **106**, 063517 (2022).
- [34] S. May, N. Dalal, and A. Kravtsov, arXiv preprint (2025), 2509.02781 [astro-ph.CO].
- [35] A. Eberhardt, M. Gosenca, and L. Hui, arXiv preprint (2025), 2510.17079 [astro-ph.CO].
- [36] S. Chandrasekhar, *Astrophys. J.* **97**, 255 (1943).
- [37] S. Chandrasekhar, *Astrophys. J.* **97**, 263 (1943).
- [38] J. Binney and S. Tremaine, *Galactic Dynamics: Second Edition*, 2nd ed. (Princeton University Press, Princeton, NJ, 2008).
- [39] L. Lancaster, C. Giovanetti, P. Mocz, Y. Kahn, M. Lisanti, and D. N. Spergel, *J. Cosmol. Astropart. Phys.* **2020**, 001 (2020), arXiv:1909.06381 [astro-ph.CO].
- [40] B. Bar-Or, J.-B. Fouvry, and S. Tremaine, *Astrophys. J.* **871**, 28 (2019), arXiv:1809.07673 [astro-ph.GA].
- [41] E. C. Ostriker, *Astrophys. J.* **513**, 252 (1999).
- [42] A. Just, F. M. Khan, P. Berczik, A. Ernst, and R. Spurzem, *Mon. Not. R. Astron. Soc.* **411**, 653 (2011).
- [43] F. Edwards, E. Kendall, S. Hotchkiss, and R. Easther, *J. Cosmol. Astropart. Phys.* **2018**, 027 (2018), arXiv:1807.04037 [astro-ph].
- [44] Y. Wang and R. Easther, *Phys. Rev. D* **105**, 063523 (2022).
- [45] R. Boey, Y. Wang, E. Kendall, and R. Easther, *Phys. Rev. D* **109**, 103526 (2024), arXiv:2403.09038 [astro-ph.CO].
- [46] R. Vicente and V. Cardoso, *Phys. Rev. D* **105**, 083008 (2022).
- [47] V. Cardoso *et al.*, *J. Cosmol. Astropart. Phys.* **07** (07), 048.
- [48] G. Agazie *et al.* (NANOGrav), *Astrophys. J. Lett.* **951**, L11 (2023), arXiv:2306.16219 [astro-ph.HE].
- [49] A. Afzal *et al.* (NANOGrav), *Astrophys. J. Lett.* **951**, L8 (2023), arXiv:2306.16213 [astro-ph.HE].
- [50] J. Antoniadis *et al.* (EPTA Collaboration), *Astron. Astrophys.* **678**, A50 (2023).
- [51] D. J. Reardon *et al.* (PPTA Collaboration), *Astrophys. J. Lett.* **951**, L6 (2023).
- [52] S. Tiruvaskar, R. Boey, R. Easther, and C. Gordon, arXiv (2025), arXiv:2512.15292 [astro-ph.CO].
- [53] M. Milosavljević and D. Merritt, *AIP Conf. Proc.* **686**, 201 (2003).
- [54] M. C. Begelman, R. D. Blandford, and M. J. Rees, *Nature* **287**, 307 (1980).
- [55] L. Z. Kelley *et al.*, *Mon. Not. R. Astron. Soc.* **471**, 4508 (2017).
- [56] F. M. Khan *et al.*, *Astrophys. J.* **773**, 100 (2013).
- [57] E. Vasiliev, F. Antonini, and D. Merritt, *Astrophys. J.* **810**, 49 (2015).
- [58] A. Gould and H.-W. Rix, *Astrophys. J. Lett.* **532**, L29 (2000).
- [59] H. Koo, D. Bak, I. Park, S. E. Hong, and J. Lee, *Phys. Lett. B* **856**, 138908 (2024).
- [60] G. Alonso-Álvarez, J. M. Cline, and C. Dewar, *Phys. Rev. Lett.* **133**, 021401 (2024).
- [61] R. Boey, E. Kendall, Y. Wang, and R. Easther, *Phys. Rev. D* **112**, 023510 (2025), arXiv:2504.16348 [astro-ph.CO].
- [62] B. C. Bromley, P. Sandick, and B. Shams Es Haghi, *Phys. Rev. D* **110**, 023517 (2024).
- [63] M. D. Weinberg, *Mon. Not. R. Astron. Soc.* **239**, 549 (1989).
- [64] M. D. Weinberg, *Astrophys. J.* **421**, 481 (1994).
- [65] M. D. Weinberg, *Mon. Not. R. Astron. Soc.* **525**, 4962 (2023), arXiv:2212.02576 [astro-ph.GA].
- [66] S. Tremaine and M. D. Weinberg, *Mon. Not. R. Astron. Soc.* **209**, 729 (1984).
- [67] J. L. Zagarac, I. Sands, N. Padmanabhan, and R. Easther, *Phys. Rev. D* **105**, 103506 (2022).
- [68] G. Agazie *et al.* (NANOGrav), *Astrophys. J. Lett.* **951**, L8 (2023), arXiv:2306.16213 [astro-ph.HE].
- [69] F. Duque, C. F. B. Macedo, R. Vicente, and V. Cardoso, *Phys. Rev. Lett.* **133**, 121404 (2024), arXiv:2312.06767 [gr-qc].
- [70] B. Schwabe, M. Gosenca, C. Behrens, J. C. Niemeyer, and R. Easther, *Phys. Rev. D* **102**, 083518 (2020), arXiv:2007.08256 [astro-ph.CO].
- [71] L. O. Téllez-Tovar, T. Matos, and J. A. Vázquez, *Phys. Rev. D* **106**, 123501 (2022), arXiv:2112.09337 [astro-ph.CO].
- [72] H.-K. Guo, K. Sinha, C. Sun, J. Swaim, and D. Vagie, *JCAP* **10** (10), 028, arXiv:2010.15977 [astro-ph.CO].
- [73] M. A. Amin, M. Jain, R. Karur, and P. Mocz, *JCAP* **08** (08), 014, arXiv:2203.11935 [astro-ph.CO].
- [74] M. Gosenca, A. Eberhardt, Y. Wang, B. Eggemeier, E. Kendall, J. L. Zagarac, and R. Easther, *Phys. Rev. D* **107**, 083014 (2023), arXiv:2301.07114 [astro-ph.CO].